The Astronomical Journal, 167:39 (31pp), 2024 January https://doi.org/10.3847/1538-3881/ad110d

A Two-Component Probability Distribution Function Describes the Mid-IR Emission from the Disks of Star-forming Galaxies

Debosmita Pathak[1], Adam K. Leroy[1,2], Todd A. Thompson[1,2,3], Laura A. Lopez[1,2,4], Francesco Belfiore[5], Médéric Boquien[6], Daniel A. Dale[7], Simon C. O. Glover[8], Ralf S. Klessen[8,9], Eric W. Koch[10], Erik Rosolowsky[11], Karin M. Sandstrom[12], Eva Schinnerer[13], Rowan Smith[14], Jiayi Sun[15,16], Jessica Sutter[12], Thomas G. Williams[17], Frank Bigiel[18], Yixian Cao[19], Jérémy Chastenet[20], Mélanie Chevance[8,29], Ryan Chown[21], Eric Emsellem[22,23], Christopher M. Faesi[24], Kirsten L. Larson[25], Janice C. Lee[25], Sharon Meidt[26], Eve C. Ostriker[27], Lise Ramambason[8], Sumit K. Sarbadhicary[1], and David A. Thilker[28]

[1] Department of Astronomy, Ohio State University, 180 W. 18th Avenue, Columbus, OH 43210, USA; pathak.89@buckeyemail.osu.edu
[2] Center for Cosmology and Astroparticle Physics, 191 West Woodruff Avenue, Columbus, OH 43210, USA
[3] Department of Physics, Ohio State University, 91 West Woodruff Avenue, Columbus, OH 43210, USA
[4] Flatiron Institute, Center for Computational Astrophysics, New York, NY 10010, USA
[5] INAF—Osservatorio Astrofisico di Arcetri, Largo E. Fermi 5, I-50157, Firenze, Italy
[6] Instituto de Alta Investigación, Universidad de Tarapacá, Casilla 7D, Arica, Chile
[7] Department of Physics and Astronomy, University of Wyoming, Laramie, WY 82071, USA
[8] Universität Heidelberg, Zentrum für Astronomie, Institut für Theoretische Astrophysik, Albert-Ueberle-Straße 2, D-69120 Heidelberg, Germany
[9] Universität Heidelberg, Interdisziplinäres Zentrum für Wissenschaftliches Rechnen, Im Neuenheimer Feld 205, D-69120 Heidelberg, Germany
[10] Center for Astrophysics |Harvard & Smithsonian, 60 Garden Street, Cambridge, MA 02138, USA
[11] Department of Physics, University of Alberta, Edmonton, AB T6G 2E1, Canada
[12] Department of Astronomy & Astrophysics, University of California, San Diego, 9500 Gilman Drive, La Jolla, CA 92093, USA
[13] Max Planck Institute for Astronomy, Königstuhl 17, D-69117, Germany
[14] Jodrell Bank Centre for Astrophysics, Department of Physics and Astronomy, University of Manchester, Oxford Road, Manchester M13 9PL, UK
[15] Department of Physics and Astronomy, McMaster University, 1280 Main Street West, Hamilton, ON L8S 4M1, Canada
[16] Canadian Institute for Theoretical Astrophysics (CITA), University of Toronto, 60 St George Street, Toronto, ON M5S 3H8, Canada
[17] Sub-department of Astrophysics, Department of Physics, University of Oxford, Keble Road, Oxford OX1 3RH, UK
[18] Argelander-Institut für Astronomie, Universität Bonn, Auf dem Hügel 71, D-53121 Bonn, Germany
[19] Max-Planck-Institut für Extraterrestrische Physik (MPE), Giessenbachstr. 1, D-85748 Garching, Germany
[20] Sterrenkundig Observatorium, Ghent University, Krijgslaan 281-S9, B-9000 Gent, Belgium
[21] Department of Physics & Astronomy, University of Western Ontario, London, ON N6A 3K7, Canada
[22] European Southern Observatory, Karl-Schwarzschild-Straß 2, D-85748, Garching, Germany
[23] Univ Lyon, Univ Lyon1, ENS de Lyon, CNRS, Centre de Recherche Astrophysique de Lyon UMR5574, F-69230, Saint-Genis-Laval, France
[24] Department of Physics, University of Connecticut, Storrs, CT 06269, USA
[25] Space Telescope Science Institute, 3700 San Martin Drive, Baltimore, MD 21218, USA
[26] Sterrenkundig Observatorium, Universiteit Gent, Krijgslaan 281 S9, B-9000 Gent, Belgium
[27] Department of Astrophysical Sciences, Princeton University, Princeton, NJ 08544, USA
[28] Department of Physics and Astronomy, The Johns Hopkins University, Baltimore, MD 21218, USA
Received 2023 October 2; revised 2023 November 21; accepted 2023 November 23; published 2023 December 29

Abstract

High-resolution JWST-MIRI images of nearby spiral galaxies reveal emission with complex substructures that trace dust heated both by massive young stars and the diffuse interstellar radiation field. We present high angular (0.″85) and physical resolution (20–80 pc) measurements of the probability distribution function (PDF) of mid-infrared (mid-IR) emission (7.7–21 μm) from 19 nearby star-forming galaxies from the PHANGS-JWST Cycle 1 Treasury. The PDFs of mid-IR emission from the disks of all 19 galaxies consistently show two distinct components: an approximately lognormal distribution at lower intensities and a high-intensity power law component. These two components only emerge once individual star-forming regions are resolved. Comparing with locations of H II regions identified from Very Large Telescope/MUSE Hα mapping, we infer that the power-law component arises from star-forming regions and thus primarily traces dust heated by young stars. In the continuum-dominated 21 μm band, the power law is more prominent and contains roughly half of the total flux. At 7.7–11.3 μm, the power law is suppressed by the destruction of small grains (including PAHs) close to H II regions, while the lognormal component tracing the dust column in diffuse regions appears more prominent. The width and shape of the lognormal diffuse emission PDFs in galactic disks remain consistent across our sample, implying a lognormal gas column density $N(\mathrm{H}) \approx 10^{21}$ cm^{-2} shaped by supersonic turbulence with typical (isothermal) turbulent Mach numbers $\approx$5−15. Finally, we describe how the PDFs of galactic disks are assembled from dusty H II regions and diffuse gas and discuss how the measured PDF parameters correlate with global properties such as star formation rate and gas surface density.

[29] Cosmic Origins Of Life (COOL) Research DAO, coolresearch.io.

Unified Astronomy Thesaurus concepts: Interstellar medium (847); Extragalactic astronomy (506); Dust physics (2229); H II regions (694); Infrared astronomy (786); Stellar feedback (1602)

Supporting material: figure set

1. Introduction

The first high-resolution mid-infrared (mid-IR) images of galaxies from JWST (e.g., Pontoppidan et al. 2022; Lee et al. 2023) show a stunningly detailed, and very complex, picture of the dusty interstellar medium (ISM). The abundance of substructures in these images captures both the "diffuse" turbulent phase of the ISM and individual knots of young star-forming regions in galaxy centers and along the spiral arms. Characterizing the overall emission in the mid-IR from the dusty ISM at high physical resolution (20–80 pc), necessary to resolve individual star-forming regions from the surrounding ISM, is now possible for the first time outside the Local Group, and across the star-forming main sequence, using JWST. This paper presents the first high angular (0.″269–0.″85) and physical resolution (20–80 pc) measurements of the probability distribution function (PDF) of mid-IR emission (7.7–21 μm) from 19 nearby star-forming galaxies, providing useful insights into the complex origins of the mid-IR emission in galaxies.

Most of the mid-IR emission from galaxies is produced from small dust grains, including polycyclic aromatic hydrocarbons (PAHs), with increasing contribution from larger dust grains at longer wavelengths (Draine 2011; Galliano et al. 2018). The physical origin of this emission is primarily from dust reprocessing of starlight from the UV and optical into the IR. At shorter wavelengths in the mid-IR, the stochastic heating of small grains leads to strong emission features from different vibrational modes of PAH molecules (especially in two of the JWST-MIRI filters we use: F770W and F1130W at 7.7 and 11.3 μm, respectively). In addition, dust grains in thermodynamic equilibrium with very intense radiation fields, such as those close to H II regions, can emit modified blackbody spectra. This contributes to continuum dust emission at longer wavelengths beyond 20 μm (see, e.g., Draine & Li 2007; Galliano et al. 2018). In low-density regions far from strong heating sources, longer mid-IR wavelengths such as 21 μm also primarily trace stochastic heating of dust grains (Draine & Li 2001; Li & Draine 2001).

Since the processes above are sensitive to both the amount of dust and the strength of the radiation field incident on the dust, the distribution of mid-IR emission from galaxies should reflect both the underlying structure of the ISM and the location of strong heating sources (see, e.g., Sandstrom et al. 2023). Because of its complex origin, the mid-IR has been used as both a star formation rate (SFR) tracer and a gas tracer (Peeters et al. 2004; Calzetti et al. 2005; Armus et al. 2007; Chown et al. 2021). Before JWST, distinguishing emission from regions dominated by recent star formation and the surrounding medium was challenging (Li et al. 2010; Hunt et al. 2015) and was mainly possible in the Milky Way and the Local Group (for galactic observations, see, e.g., Churchwell et al. 2009; Binder & Povich 2018; for Magellanic Clouds, see Paradis et al. 2009; Lawton et al. 2010; M33: Relaño & Kennicutt 2009; Relaño et al. 2018).

JWST at last offers the resolution to distinguish star-forming regions from the diffuse ISM in normal star-forming galaxies beyond the Local Group ($d \sim 10$ Mpc). Studying nearby galaxies at such high resolution provides a global view of entire systems that is not possible in the Milky Way, while still being able to well resolve star-forming regions and the turbulent ISM. With the unprecedented resolving power that JWST provides in the mid-IR, we can study star formation and baryonic feedback in the context of both its local and global environment.

Measuring PDFs of gas (column) density using multi-wavelength tracers is key to making a statistical characterization of different phases of the ISM. Due to the availability of high-resolution data, most observational studies of the structure and distribution of different phases of the ISM using PDFs of the gas (column) density of various tracers have focused on the Milky Way and other Local Group galaxies (e.g., Berkhuijsen & Fletcher 2008, 2015; Imara & Burkhart 2016; Corbelli et al. 2018 and references therein, for a galaxy-scale analysis; similarly Kainulainen et al. 2014; Schneider et al. 2022, for nearby molecular clouds). This has been complemented by high-resolution numerical simulations that establish a clear physical relation between the properties of ISM turbulence and the width and shape of the density PDF (see, e.g., Federrath et al. 2008; Hennebelle & Falgarone 2012; Molina et al. 2012; Padoan et al. 2014; Klessen & Glover 2016).

To first order, the shape of the density PDF is set by gravity and turbulence (see, e.g., Klessen & Burkert 2000; Klessen et al. 2000; Federrath & Klessen 2013; Burkhart 2018). In addition, within young star-forming regions and other active parts of the galaxy, stellar feedback such as outflows can help shape the PDFs of emission (Appel et al. 2022). The PDFs of individual giant molecular clouds (GMCs) in extinction appear primarily lognormal with a power law, which mainly reflects the superposition of gas column distributions from both turbulent bulk gas and self-gravitating cores (see, e.g., Chen et al. 2018). However, for PDFs of IR emission on large (galaxy) scales, a lognormal and power law shape is expected to be a convolution of the distribution of radiation intensity with the distribution of gas column (see Dale et al. 2001; Draine & Li 2007, for galactic IR spectral energy distributions (SEDs) and dust models). Both dust extinction and IR emission PDFs have been widely studied as tracers of gas (hydrogen) column density at very high resolution within a galactic context (e.g., Goodman et al. 2009; Lada et al. 2017; Schneider et al. 2022, and references therein). However, high-resolution IR observations of external galaxies are necessary to extend this framework to galaxies with a diversity of global properties beyond the Local Group.

In this paper, we measure the PDFs of mid-IR intensity in four JWST bands: 7.7, 10, 11.3, and 21 μm (F770W, F1000W, F1130W, and F2100W, respectively). All four bands are expected to be dominated by dust emission, with PAH features contributing most of the emission at 7.7 and 11.3 μm, while the thermal dust continuum dominates at 10 and 21 μm (Whitcomb et al. 2023b). Our goal is to make a statistical characterization of the mid-IR emission from external galaxies when observed at high enough resolution to distinguish individual star-forming regions from the surrounding ISM. We do this by parameterizing the PDFs of mid-IR intensity and corresponding gas (column) density in the first 19 nearby galaxies from the PHANGS-JWST Cycle 1 Treasury survey that span a range of

Table 1
Target Specifications and Global Properties

Galaxy	R.A. (deg)	Decl. (deg)	i[a] (deg)	D[a] (Mpc)	res.[b] (pc)	A[c] ($\times 10^4$ arcsec^2)	$\log M_*$[b] ($\log M_\odot$)	log SFR[b] ($\log M_\odot$ yr^{-1})	AGN[d]	Type[e]	Bar[e]	Center[f] ($<c$ kpc)
NGC 0628	24.17	15.78	8.9	9.8	40.5	1.6	10.3	0.2	⋯	SA(s)c	⋯	⋯
NGC 1087	41.60	−0.50	42.9	15.9	65.3	2.7	9.9	0.1	⋯	SB(rs)c_d_pec	✓	⋯
NGC 1300	49.92	−19.41	31.8	19.0	78.3	1.7	10.6	0.1	⋯	(R')SB(s_bl_nrl)b	✓	1.0
NGC 1365	53.40	−36.14	55.4	19.6	80.6	3.3	11.0	1.2	S1.8	(R')SB(r_s_nr)bc	✓	3.0
NGC 1385	54.37	−24.50	44.0	17.2	71.0	3.2	10.0	0.3	⋯	SB(s)dm_pec	✓	3.0
NGC 1433	55.51	−47.22	28.6	18.6	76.8	1.1	10.9	0.1	⋯	(R_1_')SB (r_p_nrl_nb)a	✓	1.0
NGC 1512	60.98	−43.35	42.5	18.8	77.6	3.3	10.7	0.1	⋯	(R_L)SB(r_bl_nr)a	✓	1.0
NGC 1566	65.00	−54.94	29.5	17.7	72.9	2.8	10.8	0.7	S1.5	(R_1_')SAB(rs_r_s)b	✓	1.0
NGC 1672	71.43	−59.25	42.6	19.4	79.9	2.6	10.7	0.9	S	(R')SA_B(rs_nr)b	✓	1.0
NGC 2835	139.47	−22.35	41.3	12.2	50.4	2.0	10.0	0.1	⋯	S/IB(s)m, SB(rs)c	✓	⋯
NGC 3351	160.99	11.70	45.1	10.0	41.0	1.9	10.4	0.1	⋯	(R')SB(r_bl_nr)a	✓	1.0
NGC 3627	170.06	12.99	57.3	11.3	46.6	2.7	10.8	0.6	S3	SB_x_(s)b_pec	✓	1.0
NGC 4254	184.71	14.42	34.4	13.1	54.0	2.3	10.4	0.5	⋯	SA(s)c_pec	⋯	3.0
NGC 4303	185.48	4.47	23.5	17.0	70.0	2.7	10.5	0.7	S2	SAB(rs_nl)b_c	✓	1.0
NGC 4321	185.73	15.82	38.5	15.2	62.7	2.7	10.8	0.6	⋯	SAB(rs_nr_nb)bc	✓	1.0
NGC 4535	188.58	8.20	44.7	15.8	65.0	3.2	10.5	0.3	⋯	SAB(s)c	✓	1.0
NGC 5068[g]	199.73	−21.04	35.7	5.2	21.4	1.7	9.4	−0.6	⋯	SB(s)d	✓	⋯
NGC 7496	347.45	−43.43	35.9	18.7	77.1	2.6	10.0	0.3	S2	(R')SB_x_(rs)b	✓	1.0
IC 5332[g]	353.61	−36.10	26.9	9.0	37.1	1.1	9.7	−0.4	⋯	S_AB(s)cd	✓	⋯

Notes.
[a] Galaxy inclinations adopted from Lang et al. (2020) and Leroy et al. (2021).
[b] Galaxy distances adopted from Anand et al. (2021), and stellar masses and SFRs adopted from Leroy et al. (2021) and assume a Chabrier (2003) initial mass function.
[c] The physical resolution for each galaxy corresponding to the presented common convolved angular resolution of 0.85", and the total area of the JWST-MIRI footprint with VLT-MUSE coverage over which analysis is performed for each target.
[d] AGN type, if present, for each galaxy from Veron-Cetty & Veron (2010).
[e] Comprehensive de Vaucouleurs revised Hubble−Sandage (CVRHS) types and flags noting the presence or absence of a morphologically and kinematically identified bar, respectively, in each galaxy (de Vaucouleurs et al. 1991; Makarov et al. 2014; Buta et al. 2015).
[f] Morphologically identified central regions used in this paper to measure PDFs for each galaxy, for the purposes of separating the central emission from the disk. This distinction is only when the center appears morphologically distinct from the disk in the MIR.
[g] Dwarf galaxies in our sample.

masses and SFRs across the star-forming main sequence of galaxies. The future availability of 55 more galaxies from the PHANGS-JWST Cycle 2 GO Program (GO-3707) will aid more robust characterization of mid-IR PDFs and correlations with global properties of an unprecedented large sample of galaxies.

The paper proceeds as follows. In Section 2, we describe the PHANGS-JWST Cycle 1 Treasury sample, mid-IR maps, and supporting Very Large Telescope (VLT)/MUSE data products (H II region masks and Hα coverage) that we use. In Section 3, we measure mid-IR intensity PDFs of each galaxy at each of the four filters. Section 3.1 describes how the overall PDFs are constructed, Section 3.2 presents the PDFs of galactic centers, and Section 3.3 shows the PDFs of galactic disks after decoupling from the galactic centers. Section 3.4 decomposes the emission from the galactic disks into star-forming (H II) regions and diffuse[30] ISM, and Section 3.5 parameterizes each PDF component. Section 3.6 compares and contrasts the mid-IR emission from the galactic centers, disk H II regions, and diffuse ISM in the disk. Section 3.7 discusses the effect of changes in resolution on the PDFs. Section 3.8 performs correlations between PDF parameters and galaxy-averaged properties of each target. In Section 4 we focus on the mid-IR emission from the H II region component, where Section 4.1 discusses the power law at 21 μm, and Section 4.2 estimates the bolometric luminosity surface density and radiation pressure in star-forming regions. In Section 5 we focus on the diffuse component, where Section 5.2 measures high-resolution gas column density PDFs at native F770W resolution (0.″269), and Section 5.3 derives upper bounds for Mach numbers of isothermal turbulence from gas column density PDFs in the diffuse ISM. Finally, Section 6 summarizes our key results and conclusions.

2. Data and Methods

2.1. PHANGS-JWST

We measure the distributions of mid-IR intensity for 19 nearby star-forming spiral galaxies observed by JWST as part of the PHANGS-JWST Cycle 1 Treasury program (GO 2107; PI: Lee; Lee et al. 2023). This program targets the same sample of galaxies observed by the PHANGS-MUSE program (Emsellem et al. 2022). Table 1 summarizes the properties of our targets, which span a range of stellar masses (from

[30] Here we use the label "diffuse" to refer to all gas outside of star-forming regions (H II regions), which includes some contribution from molecular, cold neutral, and warm neutral gas in the ISM. Note that this is different from the typical definition of diffuse gas in a Milky Way context ($N(\mathrm{H}) \lesssim 10^9$ cm^{-2}). So while our label of "diffuse" mostly captures truly diffuse material, it likely also includes some bound/self-gravitating gas. For the purposes of the analysis included in this paper, distinguishing star-forming regions from the surrounding material is sufficient.

$2.5 \times 10^9 M_\odot$ to $9.8 \times 10^{10} M_\odot$) and SFRs (from 0.3 to 16.9 $M_\odot$ yr^{-1}) on the star-forming main sequence and capture a wide diversity in morphologies and distinct local physical environments. The sample mostly consists of massive spiral galaxies, including 17 barred galaxies, 6 Seyfert galaxies, and 2 lower-mass dwarf spirals. For each galaxy, we use JWST-MIRI data from four mid-IR filters F770W, F1000W, F1130W, and F2100W, centered at 7.7, 10, 11.3, and 21 μm, respectively. Strong PAH emission complexes peak at 7.7 and 11.3 μm, while the emission at 21 μm is expected to better trace the dust continuum emission (Draine & Li 2007; Smith et al. 2007). The 10 μm band is known for silicate absorption (Hao et al. 2005; Spoon et al. 2007) and shows some intermediate behavior between PAH-tracing bands and the continuum, as noted later in Section 3.6.

Lee et al. (2023) describe the observations, reduction, and processing of the JWST-MIRI data, with updates to the processing and data validation described in T. Williams et al. (2023, in preparation). Relevant to this paper, the MIRI data are run through the standard JWST pipeline calibration, which is expected to yield an intensity scale accurate to better than 5% (Rigby et al. 2023). The MIRI images are astrometrically aligned with corresponding NIRCam observations of the PHANGS-JWST targets using bright point sources, and the NIRCam observations are in turn registered against Gaia DR3 astrometry. As a result, we expect the overall astrometric accuracy of the observations to be significantly better than the resolution at F2100W, our lowest-resolution band. The MIRI images are well aligned with the VLT/MUSE comparison data, which have astrometry derived indirectly through broadband imaging alignment (Emsellem et al. 2022). During data reduction, each MIRI frame is flux-corrected using an off-galaxy observation, and pointings toward different fields are mosaicked together by the pipeline. Because of the lack of large signal-free regions near the galaxy, the overall background level for each image is set using a simultaneously recorded off-axis MIRI background frame and previous wide-field mid-IR imaging, from either the Wide-field Infrared Survey Explorer (WISE) or Spitzer. After this procedure, the overall background level is uncertain to better than ± 0.05 MJy sr^{-1} (for more details see Lee et al. 2023; Leroy et al. 2023; T. Williams et al. 2023, in preparation).

2.2. Convolution to Matched Resolution

In order to compare the emission across different wavelengths, we convolve all four filters to a Gaussian point-spread function (PSF) following Aniano et al. (2011) to share a common angular resolution of 0.″85. We use this slightly coarser resolution than the native F2100W (0.″674), which would be the sharpest possible common resolution, in order to gain signal-to-noise ratio (S/N). Because F2100W is our lowest-resolution and noisiest band, and since the noise level drops rapidly with smoothing, this small convolution yields a significant improvement in the S/N in this band. To do this, we use PSFs appropriate for each filter generated following Perrin et al. (2014) and convolve following the approach described in Aniano et al. (2011). Targeting this fixed angular resolution results in slightly different physical resolutions depending on the distance of each target (20–80 pc), as included in Table 1. As we describe in Section 3.7, the results at the native resolution of each band largely resemble those derived at our common resolution of 0.″85.

Several of our targets include some "empty" galaxy-free regions in the image, which we use to estimate the statistical noise in the data at our common resolution. At our working resolution of 0.″85, the maps show typical noise values of 0.03, 0.04, 0.05, and 0.08 MJy sr^{-1} at F770W, F1000W, F1130W, and F2100W, respectively (for more details see T. Williams et al. 2023, in preparation). Because all galaxies have the same exposure time and observing procedure, we expect, and mostly observe, the statistical (random) noise to be relatively uniform (i.e., we find similar dispersion in "empty" galaxy-free regions) across different galaxies. In detail, the noise varies slightly across each image owing to the varying detector response, the dither pattern, and overlap among tiles, but these values still provide a good point of reference.

2.3. Decomposing Galaxies into Centers, Disks, and Star-forming Regions

In the following sections, we construct and analyze the PDFs of emission for each target. We systematically decompose each galaxy into three components. First, we identify galactic centers that show extreme mid-IR emission characterized by coherent peaks in emission (from unresolved point sources, saturation artifacts, etc.) from the central 1–3 kpc of galaxies that contribute to higher-order peaks at least 1 dex brighter than the mean intensity of the overall PDF. The radial extent of nuclear structures present in each target is included in Table 1, and their selection is discussed in detail in Section 3.2.

After removing the extreme central regions, we separate the galactic disks into star-forming and diffuse regions using masks that identify the locations and footprint of H II regions based on the observed Hα emission observed by VLT/MUSE. The MUSE data are described by Emsellem et al. (2022), and the H II region catalog creation and mask constructions are described in Groves et al. (2023; see also Santoro et al. 2022). In brief, the H II region masks are derived from Hα emission from the PHANGS-MUSE survey, which includes corrections for internal extinction using the Balmer decrement method that contrasts Hα and Hβ. A slightly altered version of HIIphot as first described in Kreckel et al. (2019) is used to identify and characterize H II regions with irregular morphology with a detection threshold in $\Sigma_{\mathrm{H}\alpha}$ at least 3σ above 1×10^7 erg s^{-1} cm^{-2} arcsec^{-2} (Groves et al. 2023). This work uses H II region masks derived from "convolved and optimized" versions of these maps from the PHANGS-MUSE data release. In these masks, individual H II regions are classified using emission-line diagnostics, and each pixel is identified as either belonging to an H II region or not (Groves et al. 2023), which we use to distinguish between diffuse and star-forming H II regions in our analysis. The angular resolutions of the convolved and optimized maps span from 0.″56 to 1.″25, with a median of 0.″92, almost the same as that of our convolved MIRI data. Therefore, we treat the masks as effectively matched in resolution to our observations and apply them as is with no further processing.

3. The PDFs of Mid-IR Emission in Galaxies

3.1. Constructing PDFs of Emission

We characterize the emission from each galaxy in each filter by constructing and parameterizing the PDFs of inclination-corrected intensities at each pixel measured in units of MJy sr^{-1}. The PDFs at each wavelength λ are constructed by

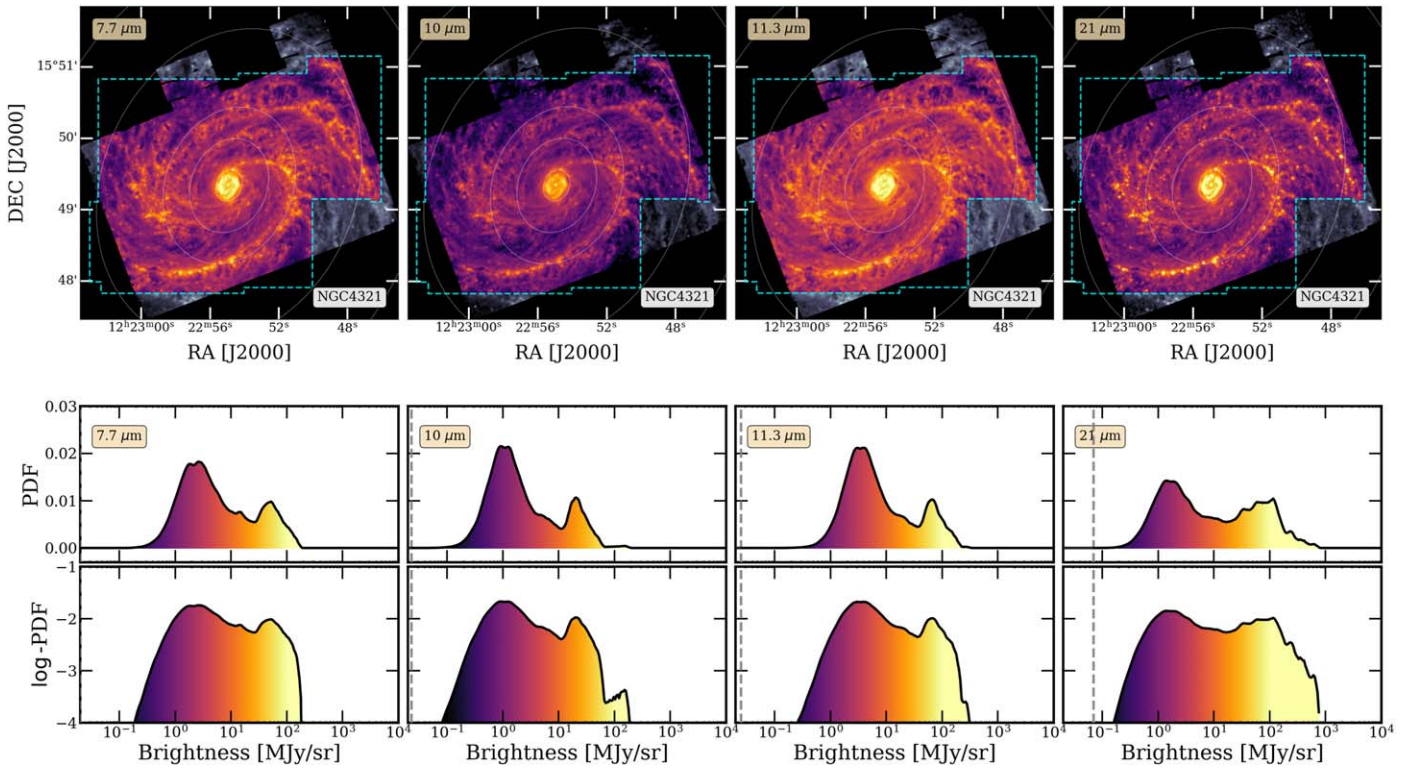

Figure 1. Images and PDFs of emission at 7.7, 10, 11.3, and 21 μm for NGC 4321 at $0\farcs85$ (60 pc) resolution. Top: JWST images for NGC 4321 in each MIRI filter, restricted to the footprint of JWST-MUSE coverage (∼10 kpc; dashed blue). Middle: PDFs of inclination-corrected intensity from each image. The colors in the PDF map to the color bar in intensity used to display each image. Vertical dashed lines indicate the rms noise level in each filter at $0\farcs85$. Bottom: the same PDF as in the middle row, but now with the *y*-axis on a logarithmic stretch to highlight features at the high-intensity end.

first dividing the mid-IR maps into logarithmically spaced bins of intensity. We then sum the total intensity I_λ (i.e., the map values) within each bin and normalize by the total intensity in the image. That is, for any intensity bin k,

$$\mathrm{PDF}(I_{\lambda_k}) = \frac{1}{\sum I_\lambda \cos i} \sum_{I_{\lambda_k}-\Delta I_\lambda/2}^{I_{\lambda_k}+\Delta I_\lambda/2} I_\lambda \cos i, \quad (1)$$

where the logarithmic bin step used to construct the histograms is typically chosen as $\Delta I_\lambda = 0.025$ dex, and i is the inclination of the galaxy (see Table 1). The PDF is in units of the fraction of total intensity, so $\sum_k I_{\lambda_k} \cos i = 1$. Figure 1 shows the PDFs of intensity for an example galaxy from our sample, NGC 4321. The PDFs show some variation in shape and intensity range across the four filters, which we discuss further in the following sections. The mid-IR images and overall PDFs of our full sample are included in Appendix A.

Note that the intensity-weighted PDFs essentially multiply the unweighted (area-weighted) PDF by the mean intensity captured in each bin. Hence, intensity-weighted PDFs better capture the contribution from regions that give rise to most of the emission, compared to pixel-wise unweighted PDFs. As a result, they are also less affected by the presence of extended galaxy-free regions in the image, uncertainties in the background level, or contributions from low-S/N regions. We prefer this luminosity-weighted PDF because most of the emission in our maps comes from regions brighter than 0.1 MJy sr^{-1} that we detect at good S/N, as is evident from Figure 1. Transforming our results back into an area-weighted PDF is a simple algebraic operation (in the limit of very fine bins, simply divide our PDF by the x-axis value), and in that case, the low-intensity end will be uncertain.

In the following sections, since our PDF intensities are detected at good S/N, we fit the binned PDF with different models. Only for display, the PDFs shown in Figure 1 and throughout this paper include a convolution with a smoothing kernel that averages over four adjacent intensity bins. However, all fit parameters reported throughout the paper (Table 2, etc.) use the original PDFs without the smoothing kernel.

3.2. Galactic Centers

As illustrated in Figure 1 and Appendix A, PDFs of overall intensity constructed using the whole JWST image tend to show both an approximately lognormal component at lower intensities and distinct, complex features at high intensity. These complex features in the PDF at high intensities can be traced back to the resolved substructure, extended JWST-MIRI PSF, and occasionally saturated pixels in the central regions. For example, in Figure 1, NGC 4321 shows a first "smooth" and broad peak at low intensity due to the disk and a second, less smooth, high-intensity peak due to emission from the center. The shapes of these high-intensity features vary dramatically across galaxies with different central sources.

These distinct features reflect the stark difference in physical conditions between the centers and disks found in some galaxies. Six out of 19 galaxies in our sample host AGNs (see Table 1 for morphological classification and AGN classes). Several galaxies host intense central star-forming environments such as nuclear star clusters and bar-fed circumnuclear rings of star formation (see, e.g., Querejeta et al. 2021; Hoyer et al. 2023; Schinnerer et al. 2023; Sormani et al. 2023). In order to

Table 2
Best-fit Parameters for Decomposed PDFs of Galactic Disks

		HII REGION MIR PDF'S[a]				DIFFUSE MIR PDF'S[b]				DIFFUSE N(H) PDF'S[c]		
Galaxy	λ (μm)	m	c (MJy sr^{-1})	ϵ_m (dex)	ϵ_c (dex)	μ (MJy sr^{-1})	σ (dex)	ϵ_μ (dex)	ϵ_σ (dex)	μ_N (cm^{-2})	σ_N (dex)	$\mathcal{M}_N$
IC 5332	7.7	−2.12	0.06	0.09	0.06	0.45	0.34	0.004	0.004	2.6×10^{20}	0.36	8.12
	10	−1.58	0.04	0.08	0.04	0.19	0.34	0.002	0.002			
	11.3	−1.93	0.05	0.06	0.05	0.73	0.30	0.004	0.004			
	21	−0.51	0.01	0.01	0.01	0.34	0.27	0.002	0.002			
NGC 0628	7.7	−1.29	0.08	0.06	0.08	2.10	0.31	0.002	0.002	1.3×10^{21}	0.33	6.42
	10	−1.33	0.03	0.02	0.03	0.92	0.30	0.002	0.002			
	11.3	−1.56	0.07	0.05	0.07	3.13	0.28	0.002	0.002			
	21	−0.35	0.02	0.01	0.02	1.32	0.32	0.002	0.002			
NGC 1087	7.7	−0.75	0.15	0.08	0.15	3.14	0.41	0.006	0.006	2.8×10^{21}	0.42	12.77
	10	−0.77	0.08	0.06	0.08	1.22	0.40	0.006	0.006			
	11.3	−0.79	0.14	0.08	0.14	4.49	0.40	0.006	0.006			
	21	−0.22	0.05	0.02	0.05	2.04	0.42	0.006	0.006			
NGC 1300	7.7	−1.92	0.23	0.20	0.23	0.61	0.44	0.003	0.003	4.5×10^{20}	0.49	21.31
	10	−1.52	0.15	0.14	0.15	0.30	0.41	0.002	0.002			
	11.3	−2.38	0.25	0.19	0.25	0.97	0.42	0.001	0.001			
	21	−0.70	0.06	0.04	0.06	0.42	0.43	0.005	0.005			
NGC 1365	7.7	−1.81	0.09	0.07	0.09	1.00	0.38	0.002	0.002	1.1×10^{21}	0.41	11.86
	10	−1.53	0.05	0.07	0.05	0.48	0.35	0.004	0.004			
	11.3	−1.92	0.15	0.12	0.15	1.61	0.35	0.003	0.003			
	21	−0.59	0.11	0.06	0.11	0.72	0.39	0.003	0.003			
NGC 1385	7.7	−0.81	0.19	0.11	0.19	2.21	0.38	0.004	0.004	2×10^{21}	0.41	11.86
	10	−0.99	0.14	0.12	0.14	0.85	0.37	0.004	0.004			
	11.3	−0.91	0.22	0.12	0.22	3.13	0.36	0.003	0.003			
	21	−0.34	0.06	0.03	0.06	1.46	0.41	0.004	0.004			
NGC 1433	7.7	−1.65	0.07	0.07	0.07	0.54	0.34	0.002	0.002	3.2×10^{20}	0.38	9.47
	10	−1.63	0.06	0.09	0.06	0.29	0.35	0.001	0.001			
	11.3	−1.79	0.11	0.09	0.11	0.90	0.35	0.002	0.002			
	21	−0.53	0.05	0.04	0.05	0.37	0.33	0.002	0.002			
NGC 1512	7.7	−1.66	0.11	0.11	0.11	0.47	0.36	0.002	0.002	3.1×10^{20}	0.41	11.86
	10	−1.21	0.06	0.08	0.06	0.25	0.36	0.001	0.001			
	11.3	−1.73	0.12	0.13	0.12	0.77	0.36	0.002	0.002			
	21	−0.63	0.04	0.04	0.04	0.33	0.37	0.003	0.003			
NGC 1566	7.7	−1.75	0.22	0.12	0.22	3.11	0.43	0.004	0.004	2.2×10^{21}	0.46	17.12
	10	−1.23	0.09	0.06	0.09	1.43	0.39	0.005	0.005			
	11.3	−1.61	0.19	0.10	0.19	4.64	0.41	0.004	0.004			
	21	−0.24	0.06	0.03	0.06	2.13	0.42	0.003	0.003			
NGC 1672	7.7	−2.51	0.19	0.12	0.19	2.45	0.40	0.004	0.004	2×10^{21}	0.43	13.75
	10	−1.41	0.09	0.06	0.09	1.05	0.37	0.004	0.004			
	11.3	−1.96	0.14	0.08	0.14	3.63	0.38	0.004	0.004			
	21	−0.47	0.04	0.02	0.04	1.70	0.41	0.004	0.004			
NGC 2835	7.7	−1.52	0.05	0.04	0.05	0.85	0.35	0.002	0.002	7.2×10^{20}	0.38	9.47
	10	−0.94	0.04	0.04	0.04	0.37	0.34	0.002	0.002			
	11.3	−1.34	0.06	0.04	0.06	1.32	0.33	0.003	0.003			
	21	−0.29	0.04	0.02	0.04	0.53	0.35	0.001	0.001			
NGC 3351	7.7	−1.47	0.03	0.03	0.03	0.64	0.27	0.001	0.001	4.8×10^{20}	0.3	5.02
	10	−1.44	0.02	0.04	0.02	0.34	0.26	0.002	0.002			
	11.3	−1.66	0.02	0.02	0.02	0.99	0.28	0.001	0.001			
	21	−0.52	0.01	0.01	0.01	0.52	0.28	0.001	0.001			
NGC 3627	7.7	−0.98	0.05	0.03	0.05	4.49	0.33	0.002	0.002	5.3×10^{21}	0.36	8.12
	10	−1.08	0.04	0.03	0.04	1.93	0.30	0.002	0.002			
	11.3	−1.33	0.10	0.04	0.10	6.67	0.32	0.002	0.002			
	21	−0.27	0.04	0.02	0.04	2.97	0.34	0.001	0.001			
NGC 4254	7.7	−1.74	0.07	0.04	0.07	3.62	0.35	0.003	0.003	3×10^{21}	0.38	9.47
	10	−1.88	0.08	0.06	0.08	1.47	0.33	0.003	0.003			
	11.3	−2.02	0.08	0.05	0.08	5.10	0.33	0.003	0.003			
	21	−0.89	0.08	0.04	0.08	2.31	0.36	0.003	0.003			
NGC 4303	7.7	−2.17	0.23	0.12	0.23	4.65	0.34	0.002	0.002	3.4×10^{21}	0.37	8.77
	10	−2.10	0.21	0.15	0.21	2.01	0.30	0.003	0.003			
	11.3	−2.43	0.32	0.17	0.32	6.94	0.32	0.002	0.002			
	21	−0.51	0.06	0.03	0.06	3.10	0.33	0.002	0.002			
NGC 4321	7.7	−1.44	0.18	0.12	0.18	2.11	0.33	0.001	0.001	1.6×10^{21}	0.36	8.12
	10	−1.35	0.05	0.04	0.05	0.96	0.29	0.001	0.001			

Table 2
(Continued)

Galaxy	λ (μm)	HII REGION MIR PDF'S[a] m	c (MJy sr^{-1})	ϵ_m (dex)	ϵ_c (dex)	DIFFUSE MIR PDF'S[b] μ (MJy sr^{-1})	σ (dex)	ϵ_μ (dex)	ϵ_σ (dex)	DIFFUSE N(H) PDF'S[c] μ_N (cm^{-2})	σ_N (dex)	$\mathcal{M}_N$
	11.3	−1.29	0.06	0.04	0.06	3.17	0.29	0.001	0.001			
	21	−0.55	0.09	0.05	0.09	1.52	0.32	0.001	0.001			
NGC 4535	7.7	−1.30	0.08	0.05	0.08	1.20	0.36	0.004	0.004	9.2×10^{20}	0.4	11.01
	10	−1.16	0.05	0.04	0.05	0.53	0.34	0.002	0.002			
	11.3	−1.32	0.12	0.07	0.12	1.74	0.34	0.002	0.002			
	21	−0.35	0.03	0.02	0.03	0.91	0.33	0.002	0.002			
NGC 5068	7.7	−1.60	0.08	0.06	0.08	1.22	0.36	0.002	0.002	7.9×10^{20}	0.39	10.21
	10	−0.91	0.03	0.03	0.03	0.52	0.34	0.002	0.002			
	11.3	−1.45	0.07	0.05	0.07	1.92	0.34	0.002	0.002			
	21	−0.08	0.02	0.01	0.02	0.73	0.36	0.001	0.001			
NGC 7496	7.7	−1.38	0.22	0.17	0.22	1.46	0.36	0.002	0.002	8.6×10^{20}	0.39	10.21
	10	−1.75	0.13	0.14	0.13	0.68	0.34	0.003	0.003			
	11.3	−1.36	0.23	0.16	0.23	2.29	0.33	0.003	0.003			
	21	−1.47	0.31	0.17	0.31	1.14	0.43	0.003	0.003			

Notes.
[a] Nonlinear regression fit parameters for the H II region power law component at each filter for each galaxy: the power law index m, logarithmic intercept c, and associated errors ϵ_m, ϵ_c, respectively, as discussed in Sections 3.4 and 4.
[b] Fit parameters for the diffuse region lognormal component at each filter for each galaxy: the lognormal mean μ, dispersion σ, and associated errors ϵ_μ, ϵ_σ, respectively, as discussed in Sections 3.4 and 5.
[c] Fit parameters for the derived N(H) gas column density PDFs in diffuse regions, as discussed in Section 5: the best-fit lognormal mean μ and dispersion σ, as well as derived average upper limits of Mach numbers $\mathcal{M}$ of isothermal turbulence.

isolate the emission from these extreme central environments, we measure the PDFs of emission from only the central 1 −3 kpc of each target, as summarized in Table 1.

The extent of the central region is selected based on the mid-IR in order to isolate extreme mid-IR emission and significant contamination from the JWST-MIRI PSF. The extent of the central region is selected based on the distribution of mid-IR emission for each galaxy with the goal of both enclosing bright emission associated with the center and isolating any artifacts associated with central sources. A number of the centers contain bright sources such as an AGN or star-forming regions in a central starburst ring. These bright compact or point sources both appear physically distinct from the disk and sometimes cause strong PSF-related artifacts, especially at F2100W. These can significantly impact our analysis (see, e.g., the center of NGC 7496 at F2100W in the Figure 18 figure set). These centers sometimes also contain areas with imperfect saturation correction (e.g., at the AGN and in the starburst ring of NGC 1365; Liu et al. 2023; S. Hannon, private communication; see the Figure 18 figure set for MIRI image). To exclude these regions, we set a radial cut that both encompasses the area where PSF wings are visible at F2100W, our lowest-resolution filter, and includes all bright emission associated with the galaxy center at this resolution. This has the risk of including some disk emission in the central regions, but we prefer this conservative approach to provide the cleanest possible characterization of the diffuse and HII region PDFs in the galactic disks. Conversely, because we weigh the PDFs by intensity, the effect of a small amount of disk contamination in the central regions will be modest. Figure 2 includes zoomed-in images and the corresponding PDFs of the central 1 kpc of NGC 4321 (see Appendix A for the full sample). While the PDFs of the central 1 kpc of NGC 4321 show a single peak in brightness, different targets show different central PDF shapes. These extreme centers can often contribute a significant fraction of the total flux in galaxies, as discussed further in Section 3.6.

In addition to capturing physically distinct environments, these central regions contain the majority of known image imperfections in our targets. The high brightness can lead to complications such as saturated pixels and diffraction spikes from the PSF associated with very bright compact sources. These complicate the interpretation of the PDFs and tend to only be present when the centers show bright emission distinct from the rest of the galactic disk. Both because of these artifacts and because the centers appear to represent a physically distinct regime, for most of this paper we separate the center from the disk and exclude these central regions from the main analysis.

In Section 3.6, we measure the flux fractions and percentiles of the intensity PDF associated with the centers, but otherwise we largely exclude the central regions from more sophisticated analysis of the PDF. Note that we do not exclude centers when the galactic centers largely resemble the rest of the galactic disks in the mid-IR. We allow this when the PDFs of the centers do not contribute additional peaks centered at $\geqslant$1 dex of the peak of the overall PDF of the galaxy. This translates to a criterion for excluding the galactic centers when the centers have a median intensity more than 1 dex higher than the median intensity in the diffuse disk component (the "peak" in the overall disk PDF). The median intensities are also reflected later in Figure 9. This is the case in NGC 0628, NGC 1087, NGC 2835, NGC 4254, NGC 5068, and IC 5332. Future works will evaluate morphological differences between the centers and disks of these targets in the optical and mid-IR.

3.3. Galactic Disks

Masking the central zone removes the high-intensity features, revealing the PDF of the disk. Figure 3 shows the disk PDFs for NGC 4321 (see Appendix A for disk PDFs of the full sample). In all four filters, these disk PDFs show a broad

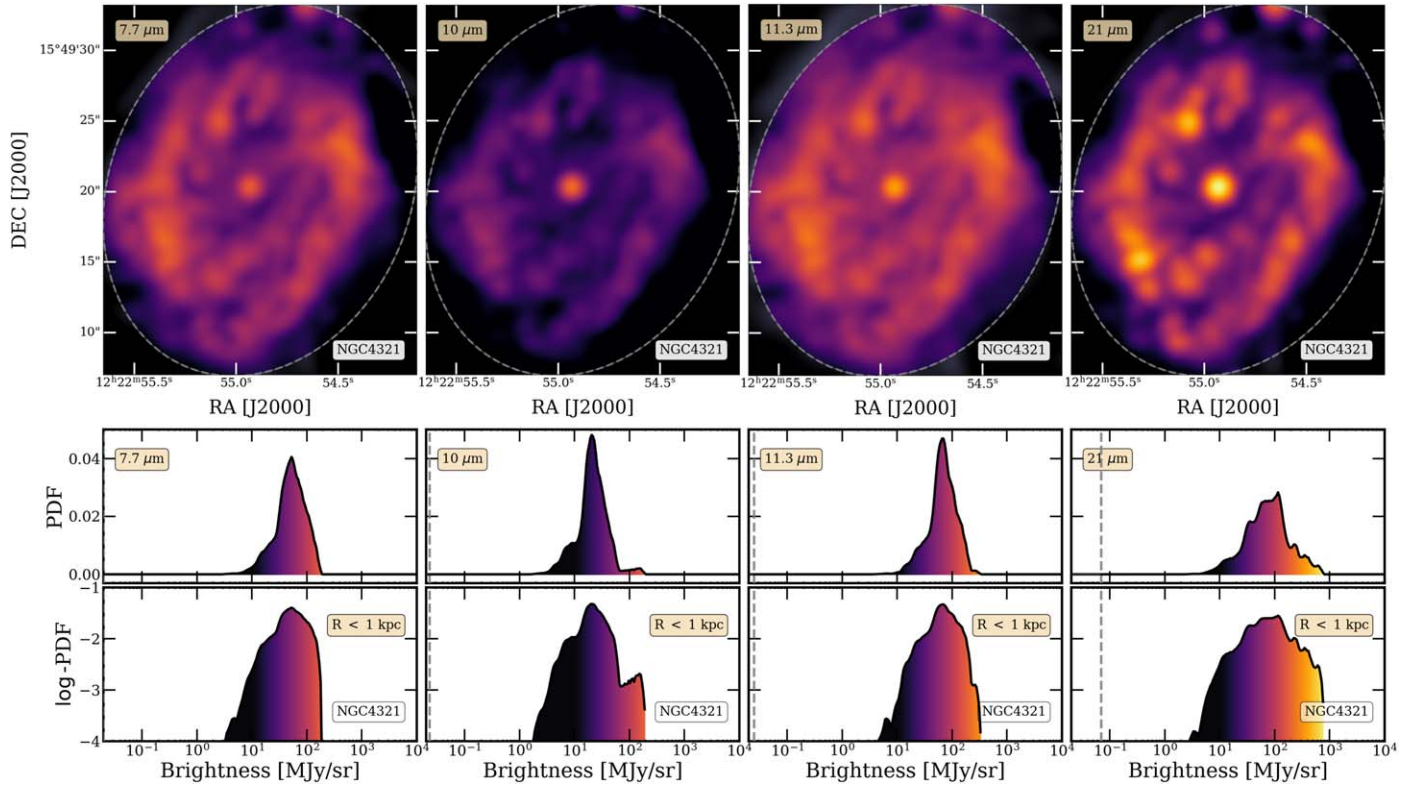

Figure 2. Images and PDFs of emission from the central 1 kpc at 7.7, 10, 11.3, and 21 μm for NGC 4321. Top: images of the central 1 kpc in NGC 4321 in each MIRI filter. Middle: pdf's of inclination-corrected intensity from each image. The colors reflect the common color bar in intensity used to display each image. Bottom: the same PDFs as in the middle row, but now with the y-axis on a logarithmic stretch to highlight features at the high-intensity end.

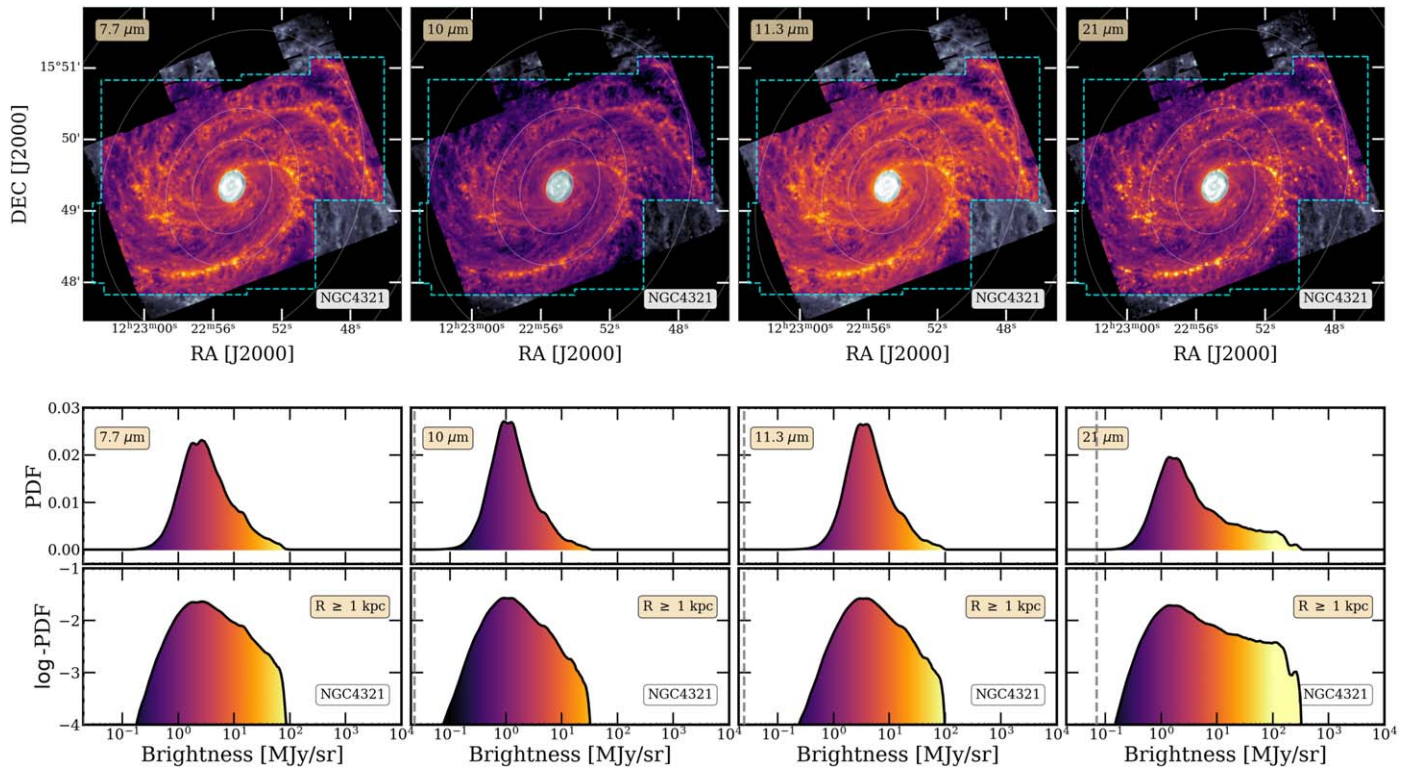

Figure 3. The PDFs of emission of the galactic disk ($r \geqslant 1$ kpc) after masking the center, at 7.7, 10, 11.3, and 21 μm for NGC 4321. Top: images of the galactic disk of NGC 4321 in each MIRI filter, with the masked central region shaded. Middle: PDFs of inclination-corrected intensity from each image excluding the masked central region. The colors in the PDF reflect the color bar in intensity used to display each image. Vertical dashed lines indicate rms noise levels in each filter. Bottom: the same disk-only PDFs shown in the middle row, but now with the y-axis in log-stretch to highlight features at the high-intensity end. The PDFs of the disk show a consistent lognormal component that peaks at lower intensities, as well as a high-intensity tail that can be roughly approximated to a power law.

peak of emission at low intensity, which appears approximately lognormal, with a continuous tail extending toward high intensity. The PDFs at F1000W and F2100W peak at lower intensities compared to the PAH-tracing F770W and F1130W filters. This is expected owing to the presence of strong PAH emission features at 7.7 and 11.3 μm. The PDFs of NGC 4321 at F770W, F1000W, and F1130W show a more prominent lognormal component, while the high-intensity tail appears more prominent and extended in the continuum-dominated F2100W filter. Nested between two strong PAH emission features, F1000W could be a tracer of either PAH bands or continuum emission. In the PDFs seen here, F1000W appears to resemble the PAH-tracing bands, featuring a more lognormal shape with lower high-intensity emission (see, e.g., Belfiore et al. 2023; Leroy et al. 2023; Sandstrom et al. 2023, for similar F1000W behavior). However, the F1000W PDFs differ from the PAH-tracing bands in some key ways—the low-intensity tail at F1000W is much more similar to the F21000W PDF, and the fall at high intensities happens at significantly lower values than PAH-tracing filters. The 9.7 μm silicate absorption feature may be a contributing factor to this intermediate behavior exhibited by the F1000W filter, as discussed in Section 3.5. Silicate absorption is most likely to be particularly important in regions of very high column density such as the galactic centers and central molecular zones (see, e.g., Lai et al. 2023, for silicate features in the center of NGC 7469). The pronounced high-intensity tail seen in the F2100W PDF is consistent with the increased thermal emissivity of the dust continuum in stronger radiation fields beyond 20 μm (e.g., Draine & Li 2007; Bendo et al. 2008; Draine 2011; Egorov et al. 2023), as discussed further in Section 4. The depression of the power-law tail at shorter wavelengths is consistent with the destruction of small dust grains (PAHs) in intense radiation fields (see, e.g., Chastenet et al. 2023a; Egorov et al. 2023).

Expanding to the full sample, Figure 4 compiles all PDFs of galactic disks at 21 μm (for brevity, see Figures 6 and 7 for PDFs using the full filter set, which all show similar shapes). It is evident that the PDFs of the galactic disks for each galaxy consistently show the same two main features we saw in NGC 4321 (Figure 3), a lognormal component that peaks at lower intensities and an approximately power law tail extending to high intensities. As a first check for this lognormal plus power law model, we fit a simple two-component model to the disk PDFs at 21 μm, the filter in which the power law is most pronounced. Due to variability in the strength of the power law, we attempt a two-part fit as

$$\text{Lognormal: PDF}(I_{\lambda_k}) = \frac{1}{\sqrt{2\pi\sigma}\, I_{\lambda_k}} e^{-\frac{(\ln I_{\lambda_k} - \mu)^2}{2\sigma^2}}, \tag{2}$$

$$\text{Powerlaw: PDF}(I_{\lambda_k}) = C I_{\lambda_k}^{m}. \tag{3}$$

To do this, we fit the low-intensity side of the peak using a lognormal, which is the dominant component. Then, we reflect and subtract this best-fit lognormal from the overall PDF. This reveals the residuals at the high-intensity end. This residual second component is well modeled by a power-law distribution, suggesting a composite shape similar to the PDF shapes of A_V in local Milky Way clouds (e.g., Lombardi et al. 2015). This suggests that more sophisticated models, like the Pareto lognormal (e.g., Hoffmann et al. 2018), could be an appropriate model to explore in future work. The 21 μm fits and associated residuals are included in Figure 4.

The errors associated with the observations are small, as reported in Section 2. The rms noise estimate for each filter is indicated on each PDF as vertical dashed lines at the low-intensity end. Since these noise estimates are small, the uniformity of the lognormal part of the distribution across bands and galaxies does not reflect noise or some other bias, but instead indicates that the mid-IR emission from diffuse regions shows a relatively universal shape across many galaxies and environments.

Following this proof of concept for describing the overall disk PDF, we devote the remainder of the paper to finding and using physically motivated independent multiwavelength ISM tracers to separate the power-law and lognormal contributions to the PDFs and performing a more rigorous parameterization of each component separately.

3.4. H II Regions and the Diffuse ISM in Galactic Disks

In Figure 4 all 19 galaxies show distinct lognormal and high-intensity power-law components in their disk PDFs. Therefore, we hypothesize that this two-component form may be a general feature of galactic disks in the mid-IR.

These two components of the PDFs of galactic disks roughly map to two spatially distinct regions in the mid-IR images of galactic disks. The high-intensity tail arises from bright spots of mid-IR emission that are often visible as compact regions near the spiral arms and bars of each galaxy. In the first four PHANGS-JWST targets, these bright point sources at 21 μm showed an excellent correspondence with the sites of recent star formation identified by Hα emission (e.g., Egorov et al. 2023; Hassani et al. 2023; Leroy et al. 2023). This suggests that the high-intensity, power-law component can be naturally explained as reflecting mostly bright, compact star-forming regions.

To test this idea, we use the H II region masks constructed in the optical from PHANGS-MUSE (Section 2). As an illustration, Figure 5 shows the disk of NGC 4303 ($R \geqslant 1$ kpc) with H II regions overlaid. The emission from the disk is then divided into emission from within (in blue) and outside of (orange) H II regions. It is clear that the H II regions identified in the optical successfully isolate the bright, approximately power-law component of the PDF, especially at the dust-continuum-tracing 21 μm. In this case, the overall high-intensity component in the PDF reflects the sum of many individual star-forming regions, which together build up the observed approximately power-law tail. The mid-IR images and overlaid H II region masks for all 19 galaxies are available in Appendix A.

Figures 6 and 7 expand this analysis to the full sample. The PDF contributions from H II regions (in blue) and the ISM outside of H II regions (in orange) are overlaid on each PDF and log-PDF for the disk of each target. It is evident from Figures 6 and 7 that this clear correspondence between the H II region masks and the distinct lognormal and power-law components of each PDF (as shown in Figure 5 for NGC 4303) extends across our whole sample. Decomposing the disks into H II and non−H II regions effectively decomposes the overall PDFs into their respective power-law and lognormal components for each target. The bright regions in the mid-IR images, the high-intensity power-law tails in the PDFs, and the H II regions identified from VLT/MUSE Hα emission are all the same to first order, as discussed further in Section 4. At shorter wavelengths, while most galaxies in Figure 7 show

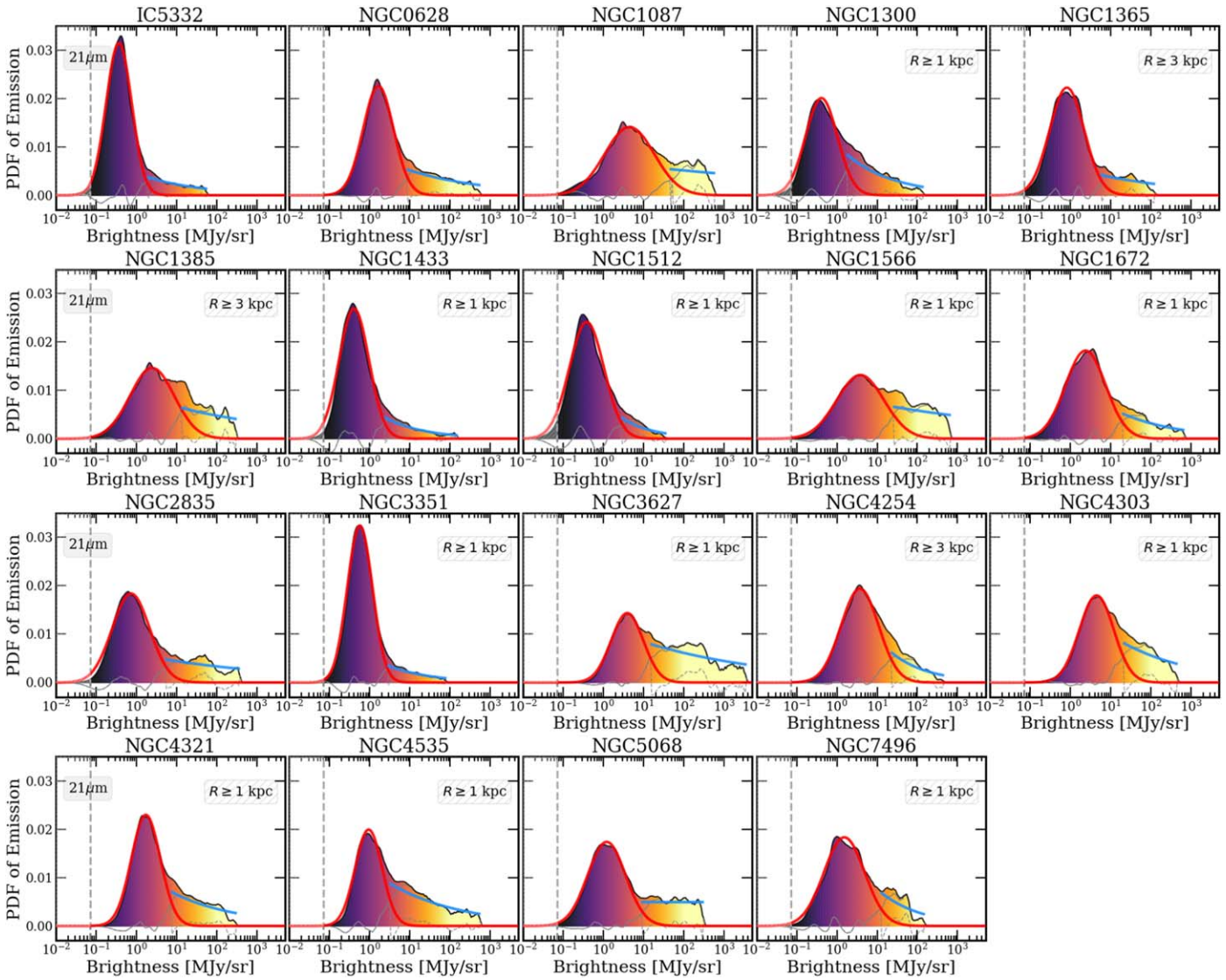

Figure 4. The PDFs of the galactic disk (in black) for our full sample at 21 μm. Vertical dashed lines show the rms noise levels for 21 μm at 0.″85. The PDFs at each filter show an overall distribution well fit by a lognormal (red) at lower intensity (residuals in gray), with high-intensity residuals (dashed gray) that are well fit by a power law (blue).

weaker but still distinguishable power-law components, the second high-density component in some galaxies could arguably also be fit by a second lognormal. However, as we discuss in Sections 3.8 and 4, since the power-law index encodes information about the luminosity function of H II regions and is pronounced at shorter wavelengths for a majority of our galaxies, we provide power-law fits to all 19 galaxies.

The emission from outside H II regions corresponds to the lognormal component of the PDF. Based on the similarity to the PDF shape expected for gas densities in a turbulent medium and the separation of these regions from strong heating sources, we suggest that this lognormal component can be identified with the "diffuse" ISM. In these regions, we expect that variations in gas and dust column density drive much of the observed shape of the PDF. The observed correlation between millimeter-wave tracers of gas column density and mid-IR emission seen in the PHANGS-JWST first results supports this interpretation (e.g., Leroy et al. 2023; Sandstrom et al. 2023). As discussed further in Section 5, this lognormal component of the PDF may constrain the column density distribution in the diffuse ISM, and thus perhaps the behavior of the turbulent ISM. Under our current definition, this includes some contribution from the cold, dense part of the ISM that is highly turbulent with supersonic Mach numbers.

In summary, while details of the PDF, such as the exact mean and width of the lognormal component, and the slope of the power-law distribution change somewhat across targets and show some systemic variation with wavelength, the overall shape of the PDFs appears similar across all 19 galaxies. This two-component behavior for galactic disks emerges across a wide range of galaxy morphologies.

3.5. Characterizing the H II Region and Diffuse Component PDFs

For the rest of this paper, we treat the PDFs of mid-IR intensity from disks as separable into diffuse and H II regions. For each galaxy, we parameterize these two distinct components by using nonlinear regression to fit a power law to the H II region and a lognormal model to the diffuse component. The power-law index m, logarithmic intercept c, and corresponding standard errors for

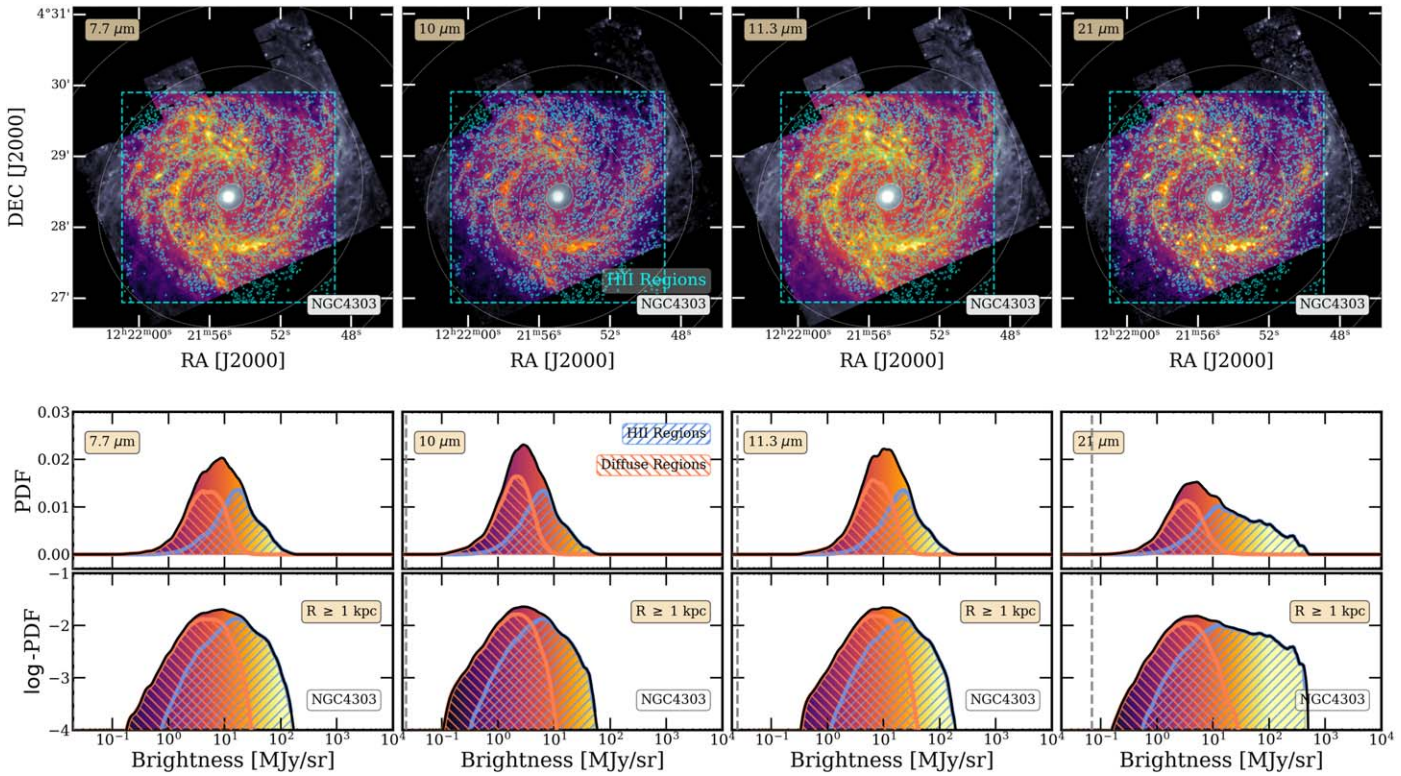

Figure 5. The PDFs of emission of the galactic disk ($r \geqslant 1$ kpc) after masking the center, at 7.7, 10, 11.3, and 21 μm for NGC 4303, tagged by emission from within and outside of H II regions. Top: images of the galactic disk of NGC 4303 in each MIRI filter, with the masked central region shaded. Hα-identified H II regions are overlaid in blue contours. Middle: PDFs of inclination-corrected intensity from the disk (excluding the masked central region), colored by the intensity color bar used to display each image. The PDFs of emission from within H II regions and outside of H II region masks are included in hatched blue and orange, respectively. Bottom: the same disk-only PDFs shown in the middle row, but now with the y-axis in log-stretch to highlight the power-law tail. It is evident that the emission from H II regions builds up the power-law component, and the diffuse ISM outside of H II regions shows a lognormal PDF.

the H II region component and the lognormal mean μ, dispersion σ, and corresponding uncertainties for the diffuse ISM component are presented in Table 2 and summarized in Figure 8 and Table 3.

As illustrated in Figure 8, the power-law slope m of the PDFs of H II regions shows a range of values between -2.5 and -0.08. At 21 μm, where the power-law component is most prominent, m shows a relatively narrow range of values, with a median index of $-0.51 \pm 0.29(\pm 1\sigma)$, corresponding to tightly clustered indices around ~ -0.5 (see Table 3 for all wavelengths). Hence, the H II region components consistently show shallow and extended power-law PDFs of intensities.

The widths of the lognormal PDFs of the diffuse regions appear largely consistent across the four filters, with a median width (lognormal dispersion) of $\sim$0.34–0.36 dex in all four filters. The width also shows relatively little scatter from galaxy to galaxy, with a standard deviation of $\sim \pm 0.039$ dex in lognormal dispersion across 7.7–11.3 μm. The lognormal widths at 21 μm show a somewhat wider spread compared to the other three filters, with a slightly larger standard deviation of $\pm$0.048 dex.

In contrast to the width, the lognormal mean μ shows some systematic variation across the four wavelengths. The diffuse component PDFs show higher mean intensities at 7.7 and 11.3 μm, where strong PAH emission complexes peak, and lower μ at 10 and 21 μm, which are expected to better trace the dust continuum. The mean also shows a larger spread in the two PAH-tracing bands ($\pm$1.3–1.9 MJy sr^{-1}, $\pm 1\sigma$), compared to the two continuum-tracing bands ($\pm$05–0.8 MJy sr^{-1}, $\pm 1\sigma$).

The galactic disk PDFs at 7.7 and 11.3 μm show similar widths and power-law indices, with slightly higher μ at 11.3 μm. The ratio of emission at 7.7 and 11.3 μm can be used to estimate the level of PAH ionization, since 7.7 μm is expected to better trace ionized PAHs, while 11.3 μm is expected to trace more neutral PAHs (see, e.g., Galliano et al. 2008; Tielens 2008; Boersma et al. 2016; Rigopoulou et al. 2021, and references therein). Chastenet et al. (2023b) find a fairly uniform population of PAHs in the disks of the first four PHANGS-JWST galaxies (NGC 0628, NGC 1365, NGC 7496, and IC 5332) based on the variations observed in the 3.3, 7.7, and 11.3 μm features. The lack of significant variation in these ratios on average across galactic disks is consistent with our PDFs of galactic disks, which do not show significant variation between 7.7 and 11.3 μm across all 19 targets.

These general trends are in good agreement with dust models and previous observational results. These models attribute most of the 7.7 and 11.3 μm emission to PAH (small-grain) bending modes. Most of the 21 μm emission is attributed to continuum emission from either stochastically heated small grains in regions of low radiation pressure or grains in thermal equilibrium in regions close to intense heating sources (Draine 2011).

Interpreting the 10 μm emission is more complicated. The 10 μm shows significantly lower intensities than 7.7 or 11.3 μm, reflecting the lack of a strong PAH emission band centered in the filter. One might be tempted to attribute the 10 μm emission primarily to continuum emission from stochastically heated very small dust grains. However, we find very different power-law slopes between 10 and 21 μm, with the 10 μm showing a steeper slope, similar to the PAH bands.

Figure 6. The galactic disk PDFs (in black) of our full sample of 19 galaxies at 7.7, 10, 11.3, and 21 μm show an overall lognormal distribution with a power-law tail at higher intensities. The power law component can be primarily attributed to emission from individual H II regions (blue), and the lognormal component comes from emission from outside H II regions (red). Vertical dashed lines indicate the rms noise level in each filter for reference. The best-fit lognormal mean μ and dispersion σ are included for each PDF.

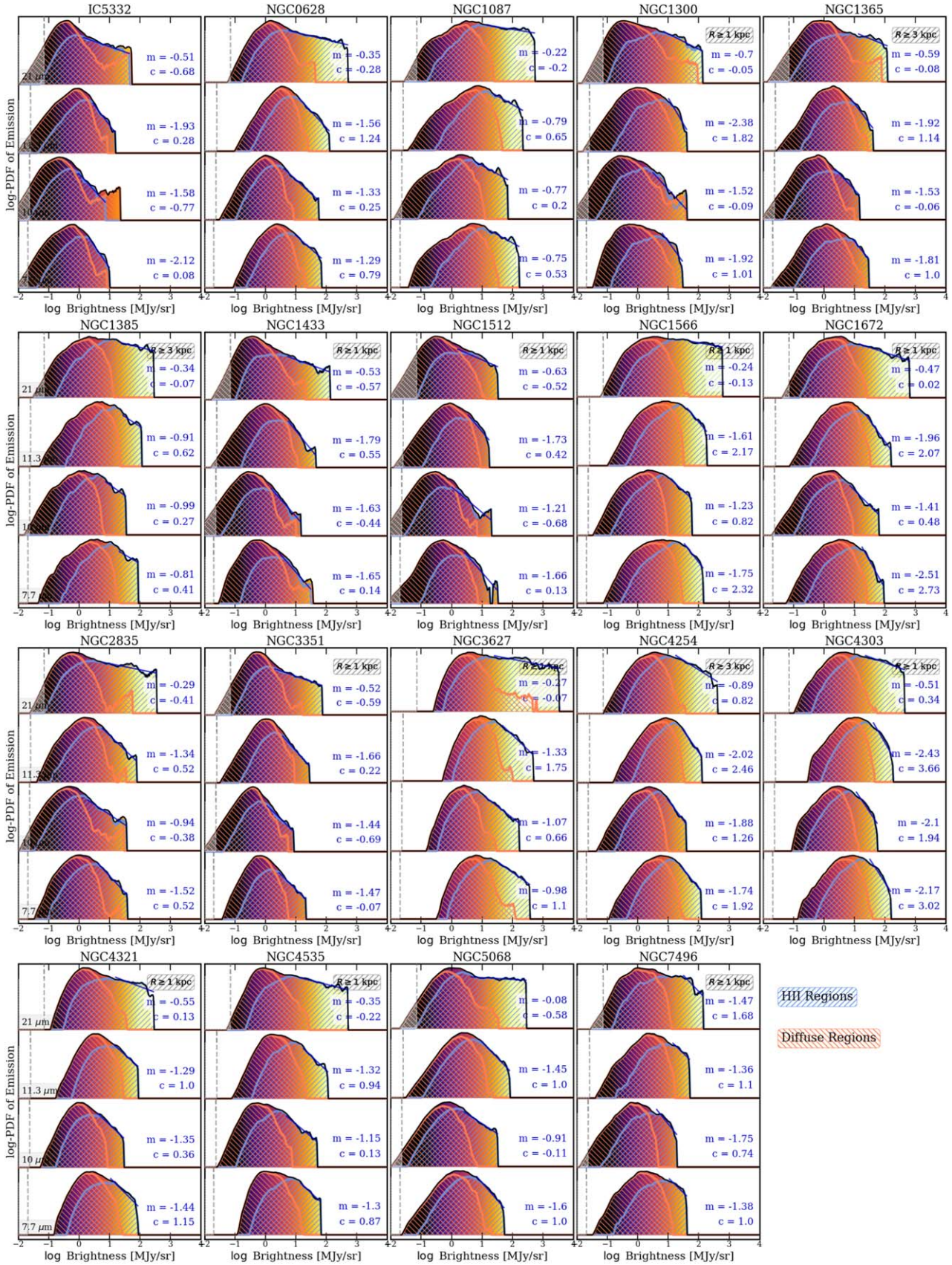

Figure 7. The disk PDFs (in black) of our sample of 19 galaxies at 7.7, 10, 11.3, and 21 μm decomposed by contributions from H II regions (blue) and outside (red). These are the same PDFs as in Figure 6, but in log-stretch to highlight the power-law component. The best-fit power law is shown in dark blue. The corresponding best-fit H II region power-law index m and log–log intercept c for each PDF are included for each panel.

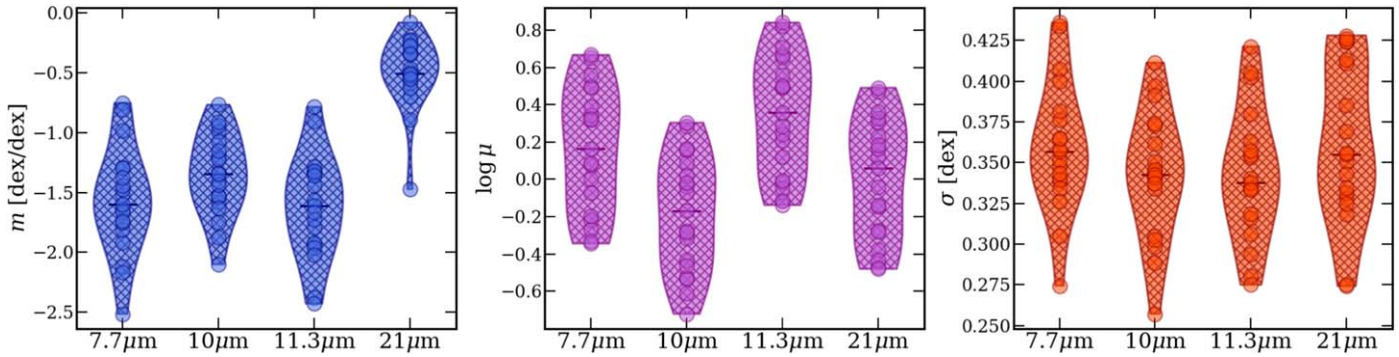

Figure 8. Summary of the galactic disk PDF parameters at each wavelength, including the H II region power-law index (m) in the left panel and the diffuse component lognormal mean (μ) and variance (σ) in the middle and right panels, respectively, as included in Table 2. The PDFs at 21 μm show significantly more pronounced power law components, while the mean intensity of the diffuse lognormal component is systematically higher in PAH-tracing 7.7 and 11.3 μm. The lognormal PDF widths remain generally consistent across the four filters.

Table 3
Summary of PDF Parameters

Best-fit Parameter	λ (μm)	Median	Q1/Q3	$\pm1\sigma$
Power law index m	7.7	−1.60	−1.78/−1.34	0.43
	10	−1.35	−1.56/−1.12	0.33
	11.3	−1.61	−1.93/−1.33	0.42
	21	−0.51	−0.57/−0.31	0.29
Lognormal mean μ	7.7	1.46	0.74/2.78	1.31
	10	0.68	0.36/1.14	0.54
	11.3	2.29	1.15/4.06	1.91
	21	1.14	0.53/1.87	0.86
Lognormal dispersion σ	7.7	0.36	0.34/0.38	0.039
	10	0.34	0.32/0.37	0.038
	11.3	0.34	0.32/0.36	0.039
	21	0.36	0.33/0.41	0.048

Note. Median, first/third quartiles, and standard deviation of the best-fit power-law index m of H II region PDFs, lognormal mean μ in MJy sr^{-1}, and dispersion σ in dex of diffuse PDFs at each filter.

The PAHs are suppressed in H II regions, likely due to the destruction of the small-grain carriers. There is also the possibility of 9.7 μm silicate absorption in the 10 μm band (Smith et al. 2007). This can uniquely affect the power-law component from H II region emission, especially since H II regions are known to have about twice the extinction compared to the more diffuse regions in the disks of normal star-forming galaxies (e.g., Calzetti 2001). Taking this all together, the 10 μm emission can best be described in our analysis as behaving "like a PAH band but fainter." Either the 10 μm filter is sensitive to silicate absorption, it captures continuum emission from PAH grains, or the small grains that produce the 10 μm continuum emission are similarly sensitive to destruction as the PAHs themselves.

All of these possibilities seem plausible. We might expect the destruction of a wide range of small grains in H II regions, which include PAHs (see, e.g., Egorov et al. 2023, and references therein). Meanwhile, the similarity in lognormal widths among all bands may similarly be attributed to PAHs being well mixed with and generally representative of small grains, which are stochastically heated in the diffuse parts of the disks. Follow-up work involving high-resolution mid-IR spectroscopy in diffuse dusty regions of nearby star-forming galaxies will be necessary to establish the nature of the emission at 10 μm and its reliability as a small-grain continuum tracer.

3.6. Contrasting the PDFs of Galactic Centers, Disk H II Regions, and the Diffuse ISM

Above, we argue that the mid-IR PDF of each target naturally breaks into three relatively distinct regimes: galactic centers, star-forming regions in disks, and diffuse emission in disks. This section quantifies and compares the distribution of flux and intensities among these three regions for each target. We show the contrast between the variability of the galactic centers and the consistency of the emission from galactic disks.

Figure 9 compares the 16th–50th–84th percentile ranges of the PDFs of the galactic centers and the two disk components of each target. Galaxies are sorted from top to bottom in order of decreasing SFR. The overall mid-IR intensity of a galaxy generally increases with increasing SFR (bottom to top), and the centers (in yellow) contrast strongly with the rest of the disk (in blue and red).[31] IC 5332, NGC 0628, NGC 2835, and NGC 5068 are exceptions, where the centers resemble the rest of the disks. The centers of AGN-classified galaxies (shown by diamonds) generally show a larger separation in intensities between the disk and center components.

Within the disks, the H II region PDFs show on average 0.5 dex higher median intensities compared to diffuse regions in the 7.7–11.3 μm range. At 21 μm, the median intensity of H II regions increases, leading to 1 dex higher median intensities on average than diffuse regions. The widths of the diffuse PDFs of emission remain broadly consistent across the full sample at all four wavelengths, as previously noted in Section 3.5. In the continuum-tracing 21 μm band, H II regions span a much broader range of intensities, translating to broader and more variable PDF widths, presumably because, unlike the PAH bands, the 21 μm captures emission from dust grains that survive in and near H II regions and are therefore exposed to a wider range of radiation fields. Finally, across all bands, the centers show highly variable PDF widths, reflecting the wide variety of substructure and environments found in galaxy centers.

The variation in both intensity and physical extent among the three region types also leads to variation in the fraction of total

[31] While the trend of increasing overall intensities with increasing SFR presented in Figure 9 is not very strong, the trend is much weaker when arranging targets in order of stellar mass or specific SFR (sSFR). This is also reflected in Figure 13, where overall intensity terms such as μ (lognormal mean intensity), median intensity in centers, H II regions, and the diffuse ISM all correlate moderately with the SFR and $\Sigma_{\rm SFR}$ but show only weak correlations with M_* and hence with sSFR.

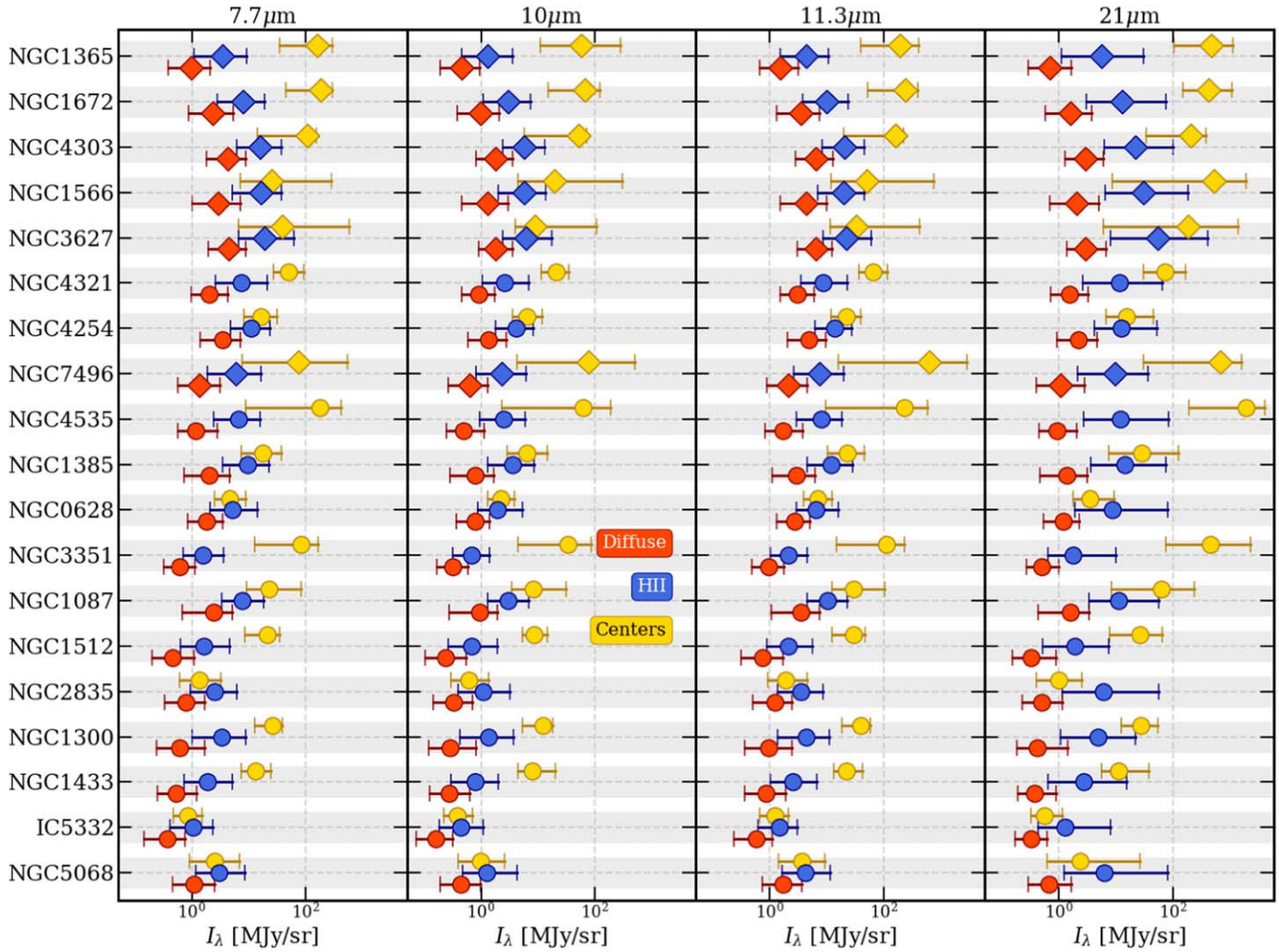

Figure 9. Median and 16th–84th range of mid-IR intensities in the diffuse ISM (red), H II region (blue), and central components (yellow) at 7.7, 10, 11.3, and 21 μm. AGN-classified galaxies (see Table 1 for AGN classification) are represented with diamonds. Targets are arranged in decreasing order of SFR from top to bottom. The overall brightness of both the disk and centers generally increases with SFR. The H II regions and centers ("bright" regions) show a significantly larger dynamical range of intensities at 21 μm.

flux coming from each region type. We plot these flux fractions for each region and each galaxy in Figure 10. Barred galaxies hosting massive bar-fed star formation complexes in the central 1–3 kpc with a limited field of view, such as NGC 1365, NGC 1385, and NGC 1672, show the highest central flux fractions. NGC 3351 is an exception that shows a comparably high intensity range for the central component despite a significantly lower SFR. This high intensity range may at least partially be attributed to NGC 3351 being closer (10 Mpc) than NGC 1365, NGC 1385, and NGC 1672 (17−20 Mpc away).

Within the extended disks, the fraction of flux from within H II regions for any given target remains roughly consistent across the four filters. On average 30% of the flux in the disk at 7.7–11.3 μm and 40% of the disk flux at 21 μm can be attributed to H II regions, while covering only 12% of the total area in the imaged disk on average. This flux fraction is in reasonable agreement with previous determinations of similar quantities in these Cycle 1 data (Belfiore et al. 2023; Leroy et al. 2023). This fraction has a weak anticorrelation with the SFR and molecular gas surface density, as we discuss next in Section 3.8. Beyond these bright star-forming regions, the emission from diffuse regions also contributes a significant fraction of the total mid-IR flux in all four filters, on average 60%–70%.

3.7. Effect of Resolution

Observing the visible power-law and lognormal components in the PDFs requires separating compact mid-IR-bright star-forming regions from the surrounding diffuse ISM. It is therefore expected that the PDF, and in particular its clear separation into these distinct components, would have an appreciable resolution dependence. The extent to which we can distinguish the power-law and lognormal components should depend on how well we can resolve individual H II regions and star-forming complexes. We demonstrate this resolution dependence in Figure 11. Starting at the native F770W (0.″269) for a representative target, NGC 0628, we convolve the native image with Gaussian kernels to progressively lower angular resolutions (following Aniano et al. 2011). We include convolutions to our lowest common native resolution at F2100W (0.″674); our slightly coarser current working resolution at 0.″85; 4.″0, comparable to the resolution of Spitzer at 8 and 24 μm bands; and 7.″5 and 15.″0, comparable to the resolution of the WISE bands 3 and 4, respectively. In

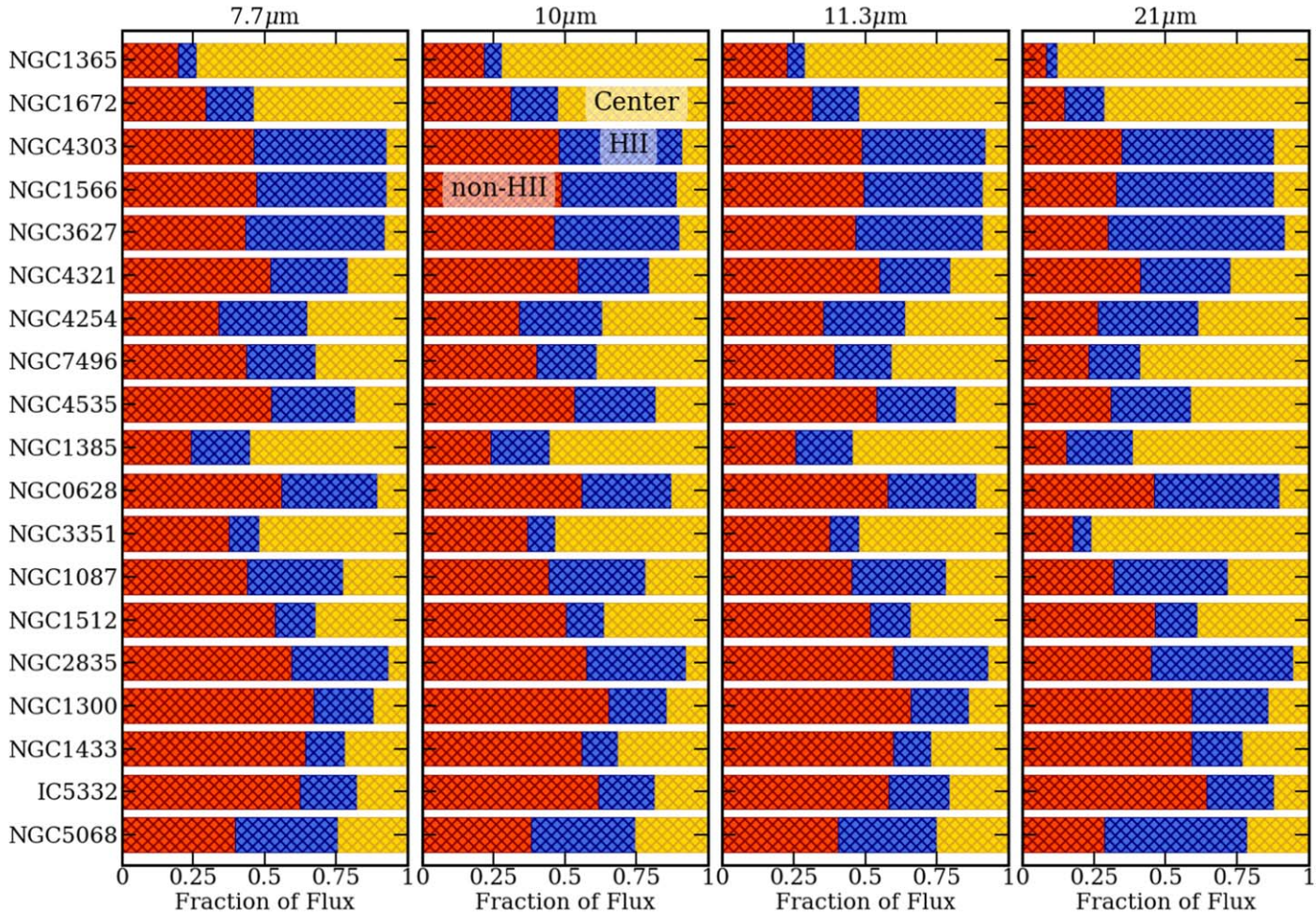

Figure 10. The fraction of total flux coming from the diffuse ISM (red), H II regions (blue), and central regions (yellow) at 7.7, 10, 11.3, and 21 μm. Targets are arranged in decreasing order of SFR from top to bottom. While the contribution from the centers varies, a significant fraction of the flux in the disk comes from diffuse emission.

NGC 0628, these angular resolutions correspond to physical resolutions of 12, 32, 40, 190, 356, and 712 pc, respectively.

With each successive smoothing, the separation between the lognormal and power law components of the PDF is blurred. As the resolution in the mid-IR drops below where we can physically resolve the mean separation between GMCs and H II regions in star-forming disks, of order 100–300 pc (see, e.g., Chevance et al. 2020; Kim et al. 2022), the power-law component is no longer visible. Below a physical resolution of a few hundred parsecs, the overall distribution of intensities collapses to a single narrow peak. This is especially evident in Figure 12, which shows convolved images of NGC 0628 at F2100W, where the power-law component is most prominent at native F2100W (32 pc resolution). At lower resolution ($\gtrsim$200 pc), the PDFs of H II and diffuse regions overlap and occupy the same region in intensity space. This is analogous to the observed spatial decorrelation between molecular gas and high-mass star formation (CO and Hα) on the scale of GMCs (here: higher-resolution, two-component PDF) and their tight correlation on galactic scales (here: lower-resolution, single-peaked PDF; e.g., Onodera et al. 2010; Schruba et al. 2010; Kruijssen et al. 2019; Chevance et al. 2020; Kim et al. 2022; Pan et al. 2022). It is evident that the two-component PDF of galactic disks only emerges at high enough angular resolution needed to achieve very high physical resolution ($\lesssim$200 pc) necessary to spatially decorrelate star formation from the surrounding gas in the star-forming disks of nearby galaxies. More sophisticated follow-up work using a constrained diffusion algorithm to separate the emission and compare the PDFs over different scales is currently underway.

In addition, within the 0.″269–0.″85 range (F770W, F2100W, and our common working resolution), PDF parameters such as the power-law slope, lognormal mean, and width remain stable within $< \pm 5\%$. Since the PDFs remain stable within the native F770W (0.″269) to 0.″85 range, the fits we provide in Table 2 can be reliably used to describe results at resolutions down to 0.″269.

3.8. Correlations with Global Properties

Physically, the two components of the PDFs map to star-forming regions and the diffuse ISM, and the properties of these components might be expected to depend on conditions in the host galaxy (Sections 3.2 and 3.4). We therefore check for correlations between the parameters of the mid-IR PDFs and global properties of the galaxies.

To do this, we compute Spearman's rank correlation coefficients relating the PDF parameters for the 21 μm PDF (the H II region power-law index m, the lognormal mean μ intensity, and dispersion σ) and also the median 21 μm brightness and flux fraction associated with the center, disk

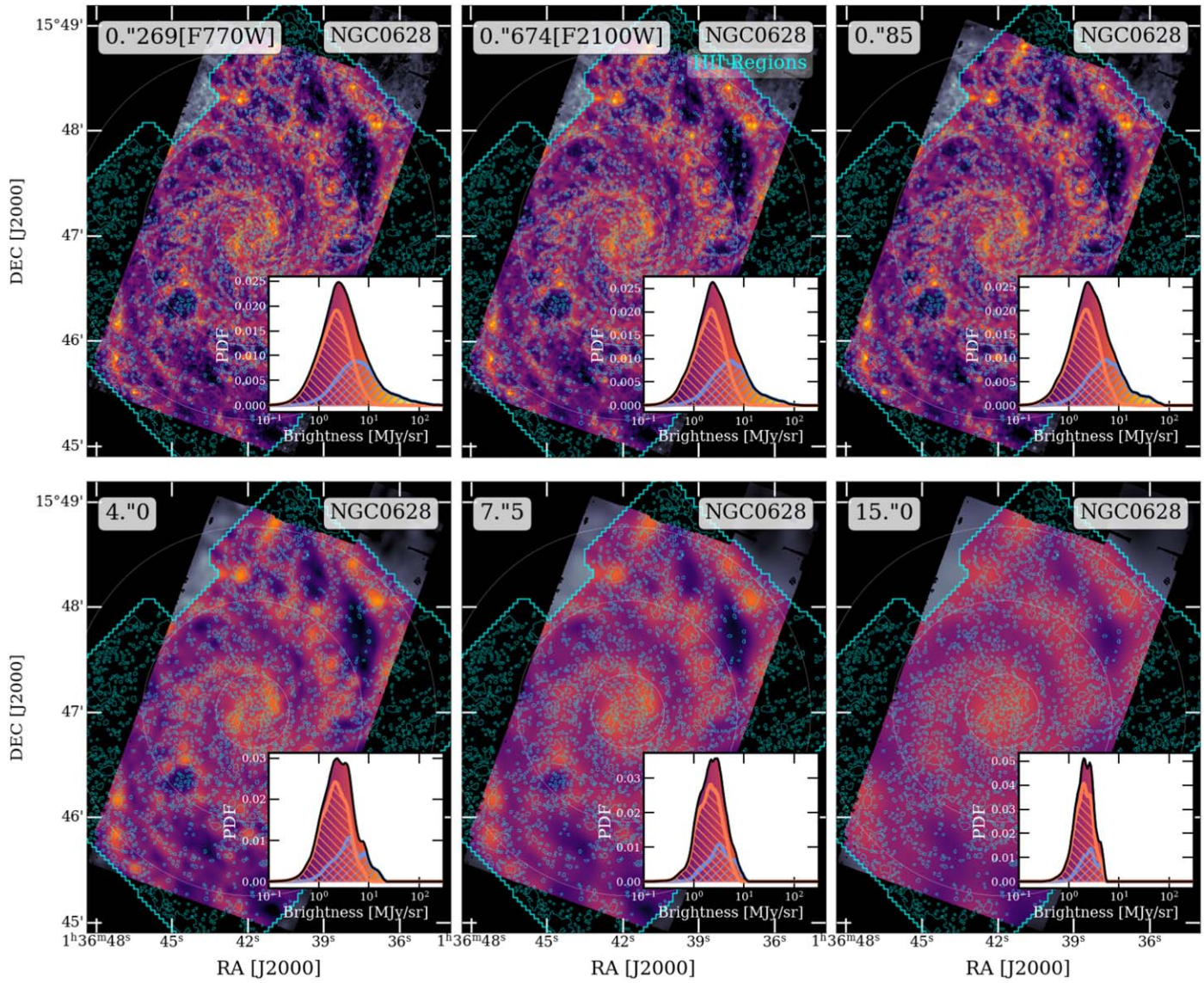

Figure 11. 7.7 μm images and PDFs of the galactic disk of NGC 0628 convolved to progressively lower resolutions—0.″269 (the native resolution of the F770W filter), 0.″674 (the native resolution of the F2100W filter), 0.″85 (our working resolution), 4.″0, 7.″5, and 15.″0. This corresponds to physical resolutions of 12, 32, 40, 190, 356, and 712 pc, respectively, in NGC 0628. The two-component PDF only emerges at high angular resolution when individual star-forming regions can be resolved from the surrounding diffuse emission.

H II regions, and diffuse ISM, to a range of different intensive and extensive global properties of the galaxies in our sample. Figure 13 presents these correlation coefficients, ρ, relating each PDF parameter at 21 μm to each target property. Higher positive values of ρ up to 1 suggest stronger correlations, and larger negative values down to -1 suggest stronger anticorrelations. The correlation coefficients at 21 μm included in Figure 13 are representative of the correlations at 7.7–11.3 μm. Since the correlation coefficients are similar across the four wavelengths and the power-law component is most prominent at 21 μm, we only include the correlations at 21 μm.

Among intensive properties, the SFR surface density $\Sigma_{\rm SFR}$ correlates most strongly with the diffuse lognormal component —including the lognormal mean and median pixel intensity— is strongly anticorrelated with the diffuse flux percentage, and shows a marginally weaker correlation with the median brightness of H II regions. The CO luminosity surface density $\Sigma_{L_{\rm CO}}$ shows similar correlations with the diffuse and H II region components (Leroy et al. 2021), while the stellar mass and H I mass surface densities $\Sigma_\star$ and $\Sigma_{M_{\rm HI}}$ do not show particularly strong correlations (Sun et al. 2022).

Among extensive properties, similar to $\Sigma_{\rm SFR}$ and $\Sigma_{L_{\rm CO}}$, the SFR and total CO luminosity $L_{\rm CO}$ show similar correlation patterns with the diffuse and H II region components. We do not find strong correlations between mid-IR PDF components and stellar mass M_*, H I gas mass $M_{\rm HI}$, mean metallicity [O/H], or effective size R_e. This is consistent with previously reported moderately strong correlations between averaged cloud-scale molecular gas properties and global galaxy properties (Sun et al. 2022). This indicates that the emission in the mid-IR is a good gas mass tracer, especially outside of H II regions, as we discuss further in Section 5.

Finally, the H II region luminosity function slope $\alpha_{\rm HII\ LF}$ (from Santoro et al. 2022) shows some interesting correlations with the components of mid-IR PDFs. $\alpha_{\rm HII\ LF}$ is the only property that the H II region power-law index shows any significant correlation with. $\alpha_{\rm HII\ LF}$ correlates moderately with the H II region power-law index and flux contribution and correlates strongly with the median

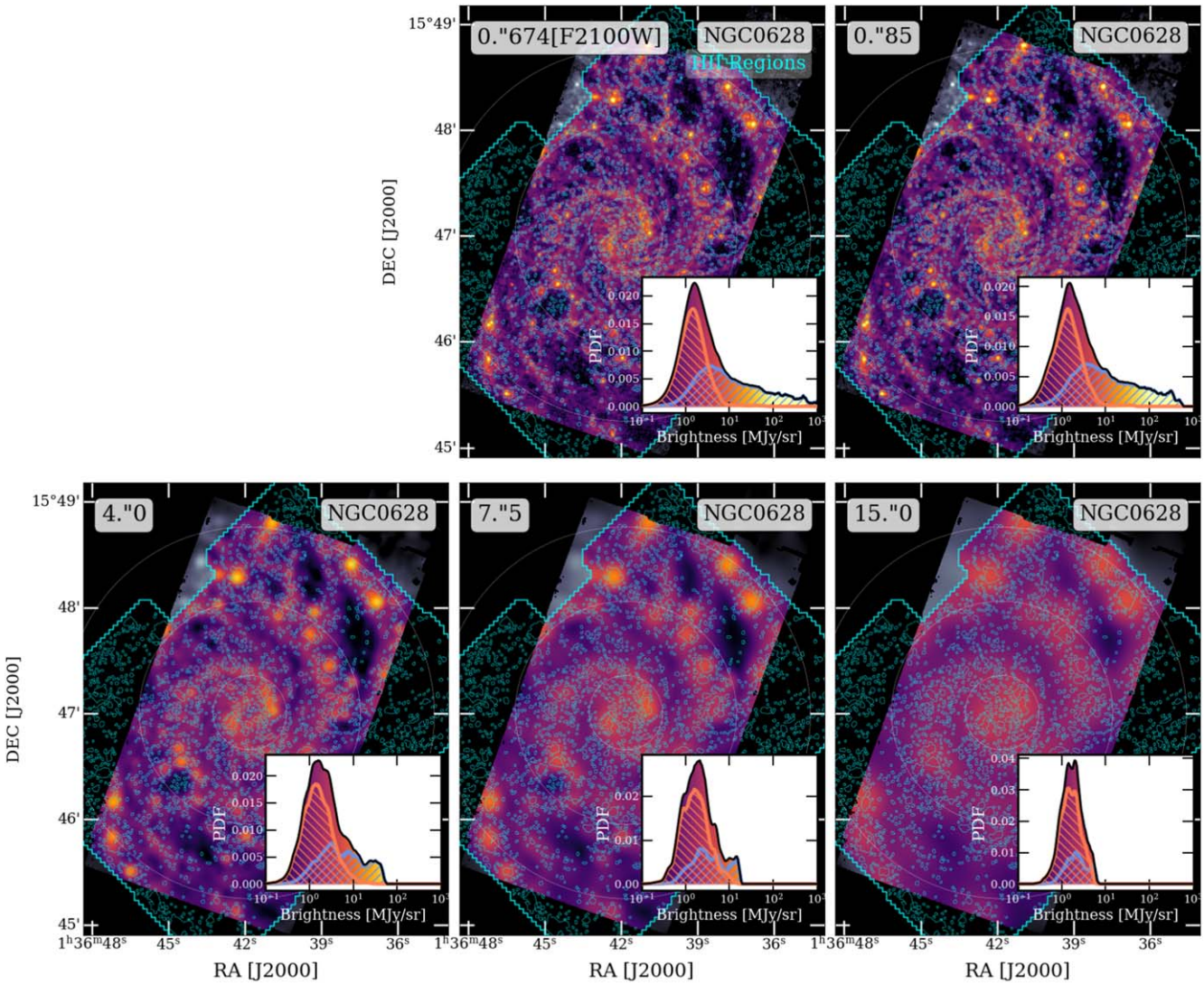

Figure 12. 21 μm images and PDFs of the galactic disk of NGC 0628 convolved to progressively lower resolutions, similar to Figure 11—0.″674 (the native resolution of the F2100W filter), 0.″85 (our working resolution), 4.″0, 7.″5, and 15.″0. This corresponds to physical resolutions of 32, 40, 190, 356, and 712 pc, respectively, in NGC 0628. While the power law is very prominent at high resolution, the power-law component is rapidly diluted at lower resolutions that do not resolve individual star-forming regions in the disk.

H II region brightness at 21 μm and diffuse lognormal mean and median brightness in the diffuse ISM.

Note that the central flux contributions depend moderately on the size of the field of view for each target relative to the size of the galaxy, and hence the inclination i and target distance d. In addition, it becomes more difficult to separate the H II region contribution and diffuse gas contribution for more distant galaxies, since the physical resolution is lower for our fixed 0.″85 angular resolution. The moderate correlation seen between the diffuse lognormal component dispersion σ and target distance makes this evident, suggesting that galaxies at larger distances may show broadening in the lognormal PDF component from some mixing of H II region emission at lower physical resolution. This is consistent with the increased overlap in H II region and diffuse component PDFs at lower resolutions (Section 3.7). Similarly, in more highly inclined galaxies, a larger fraction of the diffuse gas may end up in front of or behind an H II region, leading to emission that is more difficult to characterize as either star-forming or diffuse. However, this does not result in significant additional broadening (no correlation), since we use inclination-corrected intensities to calculate PDFs.

Building on these results, with the subsequent availability of data on 55 more galaxies from Cycle 2 JWST observations, a dedicated future paper will perform more robust comparison of multiwavelength global properties with mid-IR emission PDFs across different scales. The paper will focus on interpreting PDF parameters in light of multiwavelength information and examining PDFs in different environments and on different spatial scales within each galaxy. The PDFs presented in this work are constructed across large (galactic) scales, which are considerably different from PDFs probing the turbulent driving scale near the disk scale height or within GMCs. Since the mid-IR is a good tracer of star formation and turbulent gas (as discussed in Sections 1 and 5.1, respectively), comparing mid-IR PDFs across different scales will also provide a key point of comparison between observations and sophisticated hydrodynamic simulations of the ISM. Finally, we devote the remainder of this paper to further analyzing and discussing the H II and diffuse components of the disk PDFs.

Figure 13. Spearman's rank correlation coefficients between the parameters of mid-IR PDFs of intensity at 21 μm and global galaxy properties. Stronger positive (negative) correlations are indicated in green (pink). We present rank correlations among the most important observation-specific parameters (galaxy inclination i, distance d), intrinsic properties (SFR surface density Σ_{SFR}, stellar mass surface density Σ_{M_*}, H I mass surface density $\Sigma_{M_{HI}}$, and CO luminosity surface density $\Sigma_{L_{CO}}$), and extrinsic properties (average SFR, total stellar mass M_*, H I mass M_{HI}, CO luminosity L_{CO}, average [O/H], and effective radius R_e), as well as the H II region luminosity function slopes α from Santoro et al. (2022), with PDF parameters (H II region power-law index m, diffuse lognormal mean μ and dispersion σ) and region-wise flux contributions (median intensity I_{50} and percent of total flux in field of view for centers, H II regions, and the diffuse ISM).

4. Mid-IR Emission from the H II Region Component

As introduced in Section 3, the emission from mid-IR bright H II regions combines to yield the high-intensity power-law component of the PDFs of galactic disks. Table 2 and Figure 8 provide the parameters of the power-law component for our full sample. Our results above show first that the optically identified H II region is able to trace areas of high mid-IR luminosity surprisingly well (in excellent agreement with Hassani et al. 2023). In detail, the power-law component has some key characteristics. First, it varies by band, appearing most prominent and extended at 21 μm. Second, the intensities observed provide a direct probe into the distribution of bolometric luminosity surface densities in H II regions (indicated by the correlation of m with $\alpha_{HII\ LF}$), both of which we discuss further.

4.1. The Power Law Component at 21 μm

The PAH-tracing 7.7 and 11.3 μm filters and the small-grain-tracing 10 μm filter (see Section 3.5 for a discussion on the complex origin of the 10 μm emission) show some key differences from the 21 μm band. PAH-tracing bands consistently show much steeper power-law slopes than the continuum-dominated 21 μm, as seen in Figures 6 and 7 and summarized in Figure 8, while the PDFs at 21 μm show significantly more pronounced power law tails that span a larger dynamic range in intensities.

This difference in the 21 μm power law may arise from two processes. First, a wide range of small dust grains, including PAHs, are destroyed in high radiation-pressure-dominated regions, which include H II regions (e.g., Chastenet et al. 2023a; Egorov et al. 2023). Second, this destruction of very small grains couples with the increased thermal emissivity of the surviving larger dust grains at longer wavelengths beyond 20 μm (Draine 2011). The former suppresses the mid-IR emission from H II regions in PAH-tracing bands, leading to steeper power law slopes across 7.7 to 11.3 μm, while the latter enhances the thermal emission from H II regions at 21 μm. Together these lead to a more pronounced and extended power-law component with a shallower index at 21 μm compared to the other bands.

Young massive star clusters (e.g., Portegies Zwart et al. 2010; Krumholz et al. 2019), H II regions (Banfi et al. 1993; Mascoop et al. 2021; Santoro et al. 2022), and GMCs (Vázquez-Semadeni & García 2001; Rosolowsky 2005; Burkhart et al. 2015) all show power law distributions in luminosity. The high physical resolution of our mid-IR images allows us to distinguish substructure at the 20–80 pc physical scale. This is roughly the physical resolution at which one or a few resolution elements make up individual H II regions. Since our resolution allows us to resolve the vast majority of individual H II regions and OB associations, the power law component from the H II region PDFs at the continuum-tracing 21 μm filter is closely related to—but is not identical to—the H II region luminosity function.

Since the power law component traces the emission from H II regions, the overall power law slope of the PDF results from summing up the emission from individual H II regions. As an illustration, Figure 14 shows the PDF contributions at 21 μm from a few of the most massive H II regions in NGC 1566 (in green) overlaid on the overall power law component (in blue). Each massive H II region shows its own characteristic shape and spans a range of intensities in PDF space. The pixel-wise nature of the PDFs constitutes a key point of distinction between the power law in PDFs and the H II region luminosity function for each galaxy. Due to the size–luminosity relation for H II regions, where brighter H II regions tend to be larger in size (i.e., each region spans more pixels) and fewer in number, while fainter regions tend to be smaller (span fewer pixels) and more numerous, the PDF power law is dominated by larger and fewer bright H II regions. This is unlike the luminosity function, where each H II region contributes a single luminosity value (number counts) irrespective of any difference in sizes. Hence, the power law components in the intensity PDFs capture to first order a convolution of the luminosity function and the size–luminosity relationship for H II regions. This is reflected in Figure 13, where the 21 μm PDF power law indices correlate moderately (Spearman's rank correlation $\rho = 0.44$) with H II region luminosity function slopes measured in the optical (Santoro et al. 2022). We find little to no correlation with the PDF power law indices at shorter wavelengths 7.7, 10, and 11.3 μm ($\rho = 0.18$, 0.14, and 0.21, respectively).

4.2. Bolometric Luminosity Surface Density and Radiation Pressure

The intensity of emission in the mid-IR directly traces a fraction of the UV and optical starlight that is reprocessed by dust grains. This is true especially at longer wavelengths like 21 μm, which captures primarily thermal emission from larger dust grains. The bolometric luminosity surface density $\Sigma_{L_{\rm bol}}$ at each pixel can thus be estimated from the observed inclination-corrected mid-IR specific intensity I_ν values as

$$\Sigma_{L_{\rm bol}} = f_{\nu_{\rm bol}} 4\pi\nu I_\nu \cos i, \tag{4}$$

where $f_{\nu_{\rm bol}}$ is the bolometric intensity correction factor such that $I_{\rm bol} = f_{\nu_{\rm bol}} \nu I_\nu$. We assume $f_{21\mu{\rm m}_{\rm bol}} \approx 5$ for H II regions.[32] While the metallicity, dust composition, overall interstellar radiation field (ISRF) strength, and exact geometry of the region can lead to variations in $\Sigma_{L_{\rm bol}}$, Equation (4) is a good first-order approximation.

Scaled to typical 21 μm intensities in H II regions for our galaxies,

$$\frac{\Sigma_{L_{\rm bol}}}{L_\odot\ {\rm pc}^{-2}} = 223.11\left(\frac{I_{21\mu{\rm m}}}{10\ {\rm MJy\ sr}^{-1}}\right)\left(\frac{\lambda}{21\ \mu{\rm m}}\right)^{-1}\left(\frac{f_{\nu_{\rm bol}}}{5}\right). \tag{5}$$

Figure 15 shows the distribution of $\Sigma_{L_{\rm bol}}$ for each target in the centers, disk H II regions, and diffuse ISM assuming $f_{21\mu{\rm m}_{\rm bol}} = 5$. Modulo large differences in SFR (such as IC 5332 and NGC 5068, which are dwarf galaxies), the median luminosity of H II regions in the disks of star-forming galaxies remains generally consistent across our sample. H II regions show typical 21 μm intensities of about 10 MJy sr^{-1} and typical bolometric luminosity surface densities of order 225 $L_\odot$ pc^{-2}.

As a tracer of thermal dust emission, the intensity of emission at 21 μm likely varies at least approximately linearly with the full bolometric intensity emerging from the young stellar population (Draine et al. 2007). This allows us to extend the analysis of $\Sigma_{L_{\rm bol}}$ to conduct preliminary force balance estimates. We can estimate the pixel-wise bolometric flux $\mathcal{F}_{L_{\rm bol}}$ through the plane of the disk as

$$\mathcal{F}_{L_{\rm bol}} = f_{\nu_{\rm bol}} \pi\nu I_\nu \cos i. \tag{6}$$

This captures the luminosity from a uniformly bright patch of sky (here, each pixel) that is incident on a plane parallel to the disk, measuring the total force or radiation pressure $F_{\rm rad}$ directed out of the plane of the disk of the galaxy. For a plane disk in a galaxy, this reduces to $\Sigma_{L_{\rm bol}} = 4\mathcal{F}_{L_{\rm bol}}$. Scaled to typical values at 21 μm for a face-on galaxy,

$$\frac{\mathcal{F}_{L_{\rm bol}}}{L_\odot\ {\rm pc}^{-2}} = 55.76\left(\frac{I_\nu}{10\ {\rm MJy\ sr}^{-1}}\right)\left(\frac{\lambda}{21\ \mu{\rm m}}\right)^{-1} \times\left(\frac{f_{\nu_{\rm bol}}}{5}\right)\left(\frac{\cos i}{1}\right). \tag{7}$$

The force due to radiation pressure can be expressed as

$$F_{\rm rad} = \frac{\kappa_{\rm gas}}{c}\frac{L_{\rm bol}}{4\pi R^2} = \frac{\kappa_{\rm gas}}{c}\mathcal{F}_{L_{\rm bol}}, \tag{8}$$

where $\kappa_{\rm gas}$ is the opacity of gas along the line of sight. Since accounting for whether the photons are absorbed or scattered will give a correction factor <2, using Equation (6), we estimate the radiation pressure in an arbitrary patch of the disk (here, each pixel) as follows:

$$P_{\rm rad} = \frac{F_{\rm rad}}{\kappa_{\rm gas}} = \frac{\mathcal{F}_{L_{\rm bol}}}{c}. \tag{9}$$

$\mathcal{F}_{L_{\rm bol}}$ thus traces the radiation pressure in different environments. Finally, comparing $\mathcal{F}_{L_{\rm bol}}$ with the Eddington luminosity of star-forming regions can indicate whether radiation pressure is the dominant mechanism of feedback. This is expected to be especially important in the central molecular zones and some of the most massive star-forming complexes along the bars of star-forming galaxies, as hosted by many galaxies in our sample.

The Eddington luminosity for a dusty region is given by $L_{\rm EDD} = \frac{4\pi G M_{\rm tot} c}{\kappa_{\rm gas}}$. The Eddington luminosity surface density can thus be expressed as follows:

$$\Sigma_{L_{\rm EDD}} = \frac{4\pi G c}{\kappa_{\rm gas}}\Sigma_{M_{\rm tot}}. \tag{10}$$

Scaled to a typical value in star-forming regions (Sun et al. 2022; Blackstone & Thompson 2023),

$$\frac{\Sigma_{L_{\rm EDD}}}{L_\odot\ {\rm pc}^{-2}} = 2612.163\left(\frac{\Sigma_{M_{\rm tot}}}{100 M_\odot\ {\rm pc}^{-2}}\right)\left(\frac{\kappa_{\rm gas}}{500\ {\rm cm}^2\ g^{-1}}\right)^{-1}. \tag{11}$$

[32] While $f_{24\mu{\rm m}_{\rm bol}} \approx$ 10–20 on galactic scales at 24 μm (Spitzer; Galametz et al. 2013), this factor is expected to be lower in H II regions because local heating by young massive (zero-age main-sequence (ZAMS)) stars leads to higher dust temperatures with more of the SED emerging in the mid-IR. On the scale of H II regions, if one extrapolates the mid-IR SFR estimators by Calzetti et al. (2007) or Belfiore et al. (2023) to the fully IR case and adopts a fiducial Starburst99 ZAMS, then $f_{21\mu{\rm m}_{\rm bol}} \approx 3-5$. Among our four filters, this estimate is most accurate at F2100W since both 21 μm (JWST) and 24 μm (Spitzer) are similar tracers of thermal emission from larger dust grains.

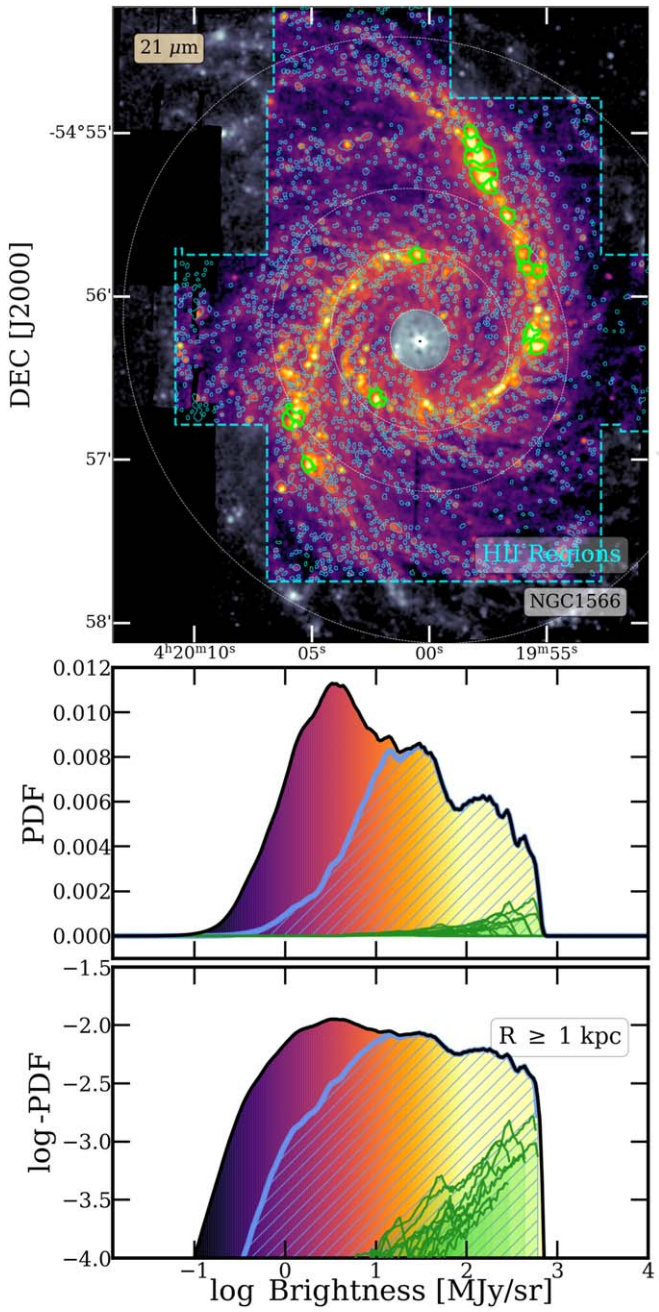

Figure 14. NGC 1566 at 21 μm with all VLT/MUSE-identified H II regions outlined in blue (top), with the corresponding PDF (middle) and log-PDF in intensity (bottom). A few of the largest H II regions in NGC 1566 are highlighted in green. The overall pdf and log-PDF of intensities at 21 μm (black), from all H II regions (blue), and each of the highlighted individual H II regions (green) are shown for comparison.

Comparing $\Sigma_{L_{\rm bol}}$, and hence $\mathcal{F}_{L_{\rm bol}}$, in different environments with this typical estimate of $\Sigma_{L_{\rm EDD}}$ in star-forming regions, Figure 15 shows that regions of diffuse emission lie comfortably below the Eddington limit, while only some of the most massive H II regions and centers come close to the typical Eddington luminosity. All six galaxies in our sample that host a central AGN (NGC 1365, NGC 1566, NGC 1672, NGC 3627, NGC 4303, and NGC 7496) have centers that exceed Eddington luminosity. The only outliers are NGC 3351 and NGC 4535, which do not host AGNs (Table 1) but show a significant amount of central emission above typical Eddington luminosities. While the actual values of Eddington luminosity surface densities in the centers may be significantly higher than the estimate in Equation (11) owing to higher $\Sigma_{M_{\rm tot}}$ in the galactic centers, it is still evident that there is significant contribution from additional feedback mechanisms beyond radiation pressure in the centers and some of the most massive star-forming regions in our sample. Future work will evaluate the correlations of force balance in star-forming regions and quiescent "diffuse" parts of the galactic disk more closely by leveraging multiwavelength information and stellar catalogs and incorporating results on $q_{\rm PAH}$, D/G, and local ionized and molecular gas fraction.

5. Mid-IR Emission from the Diffuse ISM

Simply looking at the structure of the lower-density material in mid-IR images, i.e., away from the bright H II regions and galaxy centers, reveals an inhomogeneous and apparently highly turbulent medium, which is detected almost everywhere in our images (see Appendix A for four-band images of the full sample). In Section 3.4, we found that the PDFs of mid-IR emission from diffuse regions appear lognormal. Table 2 and Figure 8 present the best-fit lognormal mean and variance fit to the diffuse emission for each band and galaxy in our sample.

The best-fit peak intensity, μ, varies from band to band in a consistent way, with higher values in the PAH-dominated 7.7 and 11.3 μm bands compared to the continuum-dominated 10 and 21 μm bands. On average, the median ratio of μ at 7.7:10:11.3:21 μm is 1.0:0.46:1.57:0.78 (Table 3). These ratios appear at least roughly consistent with the expected SED for emission from dust illuminated by a moderate ISRF (e.g., Draine et al. 2007; Draine 2011; Galliano et al. 2018), and they agree well with band ratio measurements in papers targeting the first four PHANGS-JWST galaxies (Chastenet et al. 2023a; Leroy et al. 2023) and with band ratio analysis of the full sample currently underway (J. Sutter et al. 2023, in preparation).

Meanwhile, the widths of the diffuse component PDFs, captured by the standard deviation σ, remain impressively consistent across different filters and targets, as shown in Figure 16. The common lognormal shape across bands is consistent with the idea that the different mid-IR bands mostly vary together in response to changing dust columns and radiation fields. The uniformity across targets may point to something deeper, a common distribution of ISM column density in the diffuse medium across a diverse set of galaxies.

As we discuss in the following subsections, with the assumption that mid-IR emission traces gas column density, this is in line with the gravoturbulent theory of star formation (Section 5.1), which predicts lognormal gas (column) density PDFs in the non-self-gravitating regions of the ISM (Section 5.2), with a width that is related to the rms turbulent Mach number in simple isothermal models (Section 5.3). We focus on this interpretation that the shape of the mid-IR PDF from the diffuse disk region may reflect the underlying shape of the gas column density PDF. We briefly review the motivation and mechanics for translating mid-IR intensity to gas column, and then we discuss the implications of our measurements for the gas column distribution and the Mach number. The dust likely traces both the atomic and the molecular gas with sensitivity to fairly low column densities given the high resolution (see Sandstrom et al. 2023). We emphasize the novelty of this measurement: these are some of the first

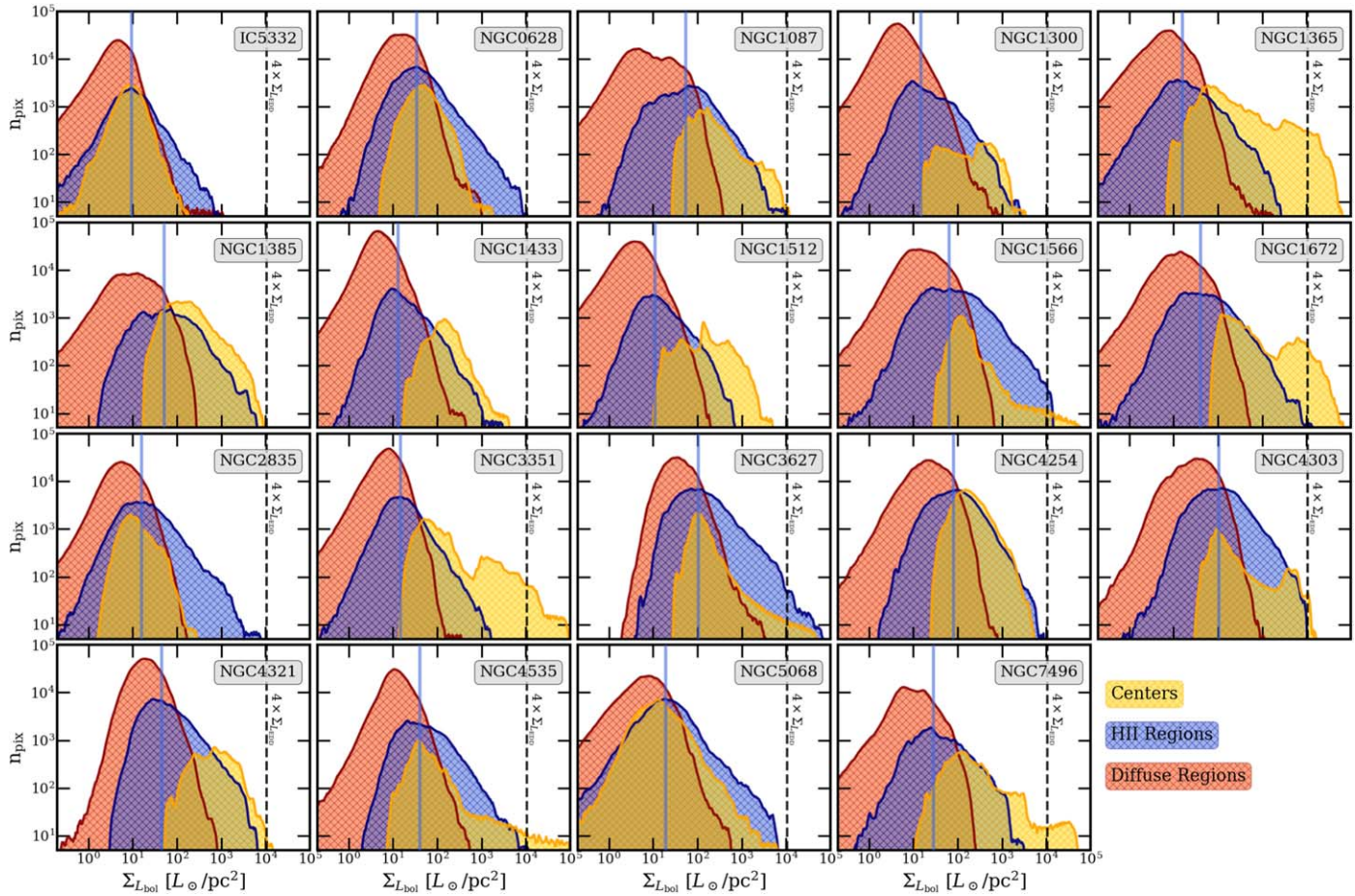

Figure 15. Histograms of pixel-wise bolometric luminosity surface density $\Sigma_{L_{bol}}$ from the center (yellow), diffuse component (red), and H II regions (blue) for each of our targets. The median $\Sigma_{L_{bol}}$ for H II regions (vertical blue line) remains roughly consistent between targets. The vertical dashed line shows the estimated Eddington luminosity surface density in star-forming regions, scaled from $\mathcal{F}_{L_{bol}}$ to $\Sigma_{L_{bol}}$ units for direct comparison.

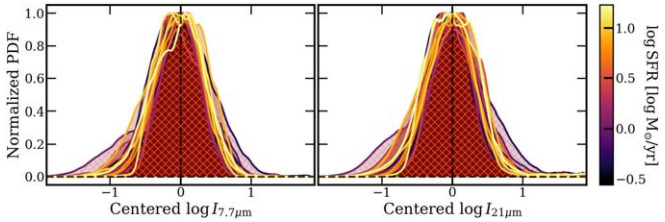

Figure 16. Stacked PDFs of emission from "diffuse" regions normalized by mean intensity and amplitude at 7.7 and 21 μm. The widths of the PDFs remain consistent across targets, with the exception of NGC 1300 with a broad PDF.

measurements to sample the shape of the PDFs of gas column density at such high resolution for galaxies outside the Local Group.

5.1. Conversion from Mid-IR Intensity to Gas Column Density

Mid-IR intensities reflect both the radiation field heating the dust and the amount of dust present, which in turn depends on the amount of gas present (e.g., Dale et al. 1999). In regions of very intense heating, the observed mid-IR intensity mostly reflects the heating term and depends on the amount of radiation absorbed by the dust. However, this situation mostly holds within H II regions and the centers of galaxies. In the more diffuse regions away from H II regions, the diffuse mid-IR emission should be a good tracer of column density, as the radiation field varies more weakly than the gas column density. This appears to be borne out by a very good local correlation between CO emission, tracing molecular gas column density, and mid-IR emission on ∼100–200 pc scales (see Whitcomb et al. 2023a; Leroy et al. 2023; Sandstrom et al. 2023). In this case, we might expect the lognormal PDFs that we observe to trace the underlying gas column density distribution and to reflect the convolution of turbulence and self-gravity in the diffuse ISM (Burkhart et al. 2017).

In regions of relatively weak radiation fields (away from H II regions), the emission in the mid-IR translates to projected gas column densities when the strength of the local IRSF, dust-to-gas ratio (D/G), and PAH fraction (q_{PAH}) are known. Based on the Draine & Li (2007), Draine et al. (2007), and Compiègne et al. (2010) dust models, as summarized in Leroy et al. (2023),

$$\frac{I_\nu^X}{\mathrm{MJy\ sr^{-1}}} \propto \left(\frac{N(\mathrm{H})}{10^{20}\ \mathrm{cm^{-2}}}\right)\left(\frac{D/G}{0.01}\right)\left(\frac{U}{U_0}\right)\left(\frac{q_{PAH}}{0.046}\right), \quad (12)$$

where I_ν^X is the mid-IR intensity for filter X and N(H) is the projected column of density of hydrogen along the line of sight. The additional parameters are D/G, the dust-to-gas mass ratio with a typical value of 0.01 from dust models of star-forming galaxies (Draine et al. 2007; Sandstrom et al. 2013; Aniano et al. 2020), and q_{PAH}, the fraction of total dust mass in PAHs, which is approximately 0.046 in Milky Way–like galaxies

(Draine & Li 2007; Draine et al. 2007). The factor of $q_{\rm PAH}$ becomes relevant for PAH-tracing bands such as F770W and F1130W. U/U_0 expresses the mean local ISRF in solar neighborhood units from Mathis et al. (1983). Directly estimating N(H) from dust modeling thus involves several moving parts, which are currently being investigated for the full sample of 19 galaxies (see, e.g., J. Sutter et al. 2023, in preparation). Future work will use these results to investigate N(H) PDFs at smaller scales across a diversity of physical environments. In the current paper, we present the PDFs of average column density in the diffuse regions of star-forming disks. Since our PDFs are constructed on large (galactic) scales, we take an alternative and more empirical approach that leverages the strong correlation between mid-IR intensities and CO (2–1) intensities.

Leroy et al. (2023) find that mid-IR emission at F770W, F1000W, F1130W, and F2100W correlates strongly with $I_{\rm CO(2-1)}$ at the 20–80 pc resolution for the first four of our targets observed (NGC 0628, NGC 1365, NGC 7496, and IC 5332), and these correlations extend to our full sample of targets (Leroy et al. 2023, in preparation). We use the fiducial empirical correlations between mid-IR intensities and $I_{\rm CO(2-1)}$ that include all 19 galaxies in our sample. The intensities at 7.7 μm show the best correlation with $I_{\rm CO(2-1)}$, where the correlation is almost linear, followed by 11.3, 10, and 21 μm, respectively (Leroy et al. 2023; A. K. Leroy et al. 2023, in preparation),

$$I_{\rm CO(2-1)} = 0.912 I_{7.7\mu{\rm m}}^{1.06}, \tag{13}$$

with the fit conducted primarily at column densities where molecular gas is expected to dominate the total gas mass. Since CO (2–1) is a widely used and robust tracer of molecular gas column density in galaxy disks (modulo subtleties with conversion factors), we subsequently estimate the projected gas column density of H using CO (2–1) intensities in units of K km s^{-1} as

$$\frac{N({\rm H})}{10^{20}\ {\rm cm}^{-2}} \approx 6.2 \left(\frac{\alpha_{\rm CO(1-0)}}{\alpha^{\rm MW}_{\rm CO(1-0)}}\right)\left(\frac{0.65}{R_{21}}\right)\left(\frac{I_{\rm CO(2-1)}}{\rm K\ km\ s^{-1}}\right), \tag{14}$$

which translates to

$$\frac{\Sigma_{M_{\rm gas}}}{M_\odot\ {\rm pc}^{-2}} \approx 1.089 \frac{N({\rm H})}{10^{20}\ {\rm cm}^{-2}}, \tag{15}$$

assuming $N({\rm H_2}) \approx 0.5N({\rm H})$ for a typical $R_{21} \equiv I_{\rm CO(2-1)}/I_{\rm CO(1-0)} = 0.65$ (den Brok et al. 2021; Yajima et al. 2021; Leroy et al. 2022) and a typical Galactic CO (1–0)–to–H_2 conversion factor of $\alpha^{\rm MW}_{\rm CO(0-1)} = 4.35\ M_\odot\ {\rm pc}^{-2}\ ({\rm K\ km\ s^{-1}})^{-1}$ (e.g., Bolatto et al. 2013).

5.2. Column Density PDF from Mid-IR Emission

The PDFs of projected gas column densities N(H) for each of our targets are presented in Figure 17. The PDFs estimate typical projected gas column densities of order $\sim 10^{21}$ cm^{-2} in the diffuse ISM of nearby galactic disks, which is consistent with current estimates for the Milky Way (see, e.g., Smith et al. 2023). Table 2 includes the best-fit lognormal mean μ_N and dispersion σ_N for the N(H) PDFs. These parameters are summarized in Table 4. These estimates use empirical correlations between $I_{\rm CO(2-1)}$ and F770W over a range of column densities where we expect $N({\rm H}) \sim 2N({\rm H_2})$. If we use similar empirical correlations from Leroy et al. (2023, in preparation) that also include low-resolution 21 cm H I imaging to estimate $N({\rm H}) = N({\rm H\,I}) + 2N({\rm H_2})$, we find $\sim$0.05 dex lower σ_N and $\sim 0.5 \times 10^{20}$ cm^{-2} higher μ_N on average, compared to the fiducial correlations using only $I_{\rm CO(2-1)}$ to estimate the gas, which yield the results reported in Table 2. The differences between the two cases can be treated as realistic uncertainties on our estimates of gas column density. The lognormal mean μ_N and dispersion σ_N of the N(H) PDFs remain consistent to within 5% and 7%, respectively, within the 0.″269–1.″0 range for all our galaxies (Appendix B).

The overall lognormal shapes of the PDFs of gas column from mid-IR intensities are also in agreement with the well-studied lognormal shape of the PDF of column densities in the turbulent gas phase of the local ISM (Vázquez-Semadeni & García 2001; Brunt et al. 2010; Federrath et al. 2010; Burkhart et al. 2015; Thompson & Krumholz 2016). In addition to observations in the Local Group and nearby galaxies (e.g., Corbelli et al. 2018), high-resolution simulations of turbulence and feedback-driven outflows predict a lognormal PDF of N(H) in turbulent diffuse gas. The lognormal shape of the PDFs emerges in simulations of isothermal turbulence and simulations that account for realistic heating and cooling in the cold neutral medium and molecular phases (see, e.g., Glover et al. 2010). Hence, the key to a lognormal gas (column) density PDF is the absence (or nondominance) of gravity, which allows supersonic turbulence to dominate the dynamics (see, e.g., Federrath et al. 2008; Girichidis et al. 2014, for analytic models). The physical origin of the lognormal shape at low densities is still debated (see, e.g., Lombardi et al. 2015), due to the difficulty in mapping out nearby molecular clouds to low extinction (A_V).

Finally, while the PDFs of molecular clouds show similar lognormal and power-law components to the overall mid-IR intensity PDFs of disks, the power law in molecular clouds emerges as a result of the dominance of self-gravity in dense cores, not as a result of heating from bright young stars, which is a key distinction.

5.3. Mach Numbers of Isothermal Turbulence

In the diffuse parts of the galactic disks, we can estimate mean turbulent Mach numbers $\mathcal{M}$ using the dispersion σ_N of the PDFs of N(H) (see Krumholz 2014, and references therein). While this involves assumptions of how the temperatures in the diffuse ISM vary spatially, our N(H) PDFs capture gas far from strong heating sources (away from centers and H II regions). These parts of the galaxies are primarily cold neutral or molecular gas dominated, showing a similar dependence of $\mathcal{M}$ on σ_N to the isothermal case. We provide upper bounds of isothermal turbulent Mach numbers, where we attribute the entire width of the N(H) PDF to turbulent broadening. Following Brunt et al. (2010) and Thompson & Krumholz (2016), we can estimate these upper bounds for isothermal ($\gamma = 1$ in $P \propto \rho^\gamma$) turbulent Mach numbers, where the dispersion σ_ρ of 3D (volumetric) gas density PDFs translates to Mach numbers of isothermal turbulence $\mathcal{M}$ as (Ostriker et al. 2001; Padoan & Nordlund 2002; Li et al. 2003; Thompson & Krumholz 2016)

$$\sigma^2_{\ln \rho} \approx \ln(1 + \mathcal{M}^2/4), \tag{16}$$

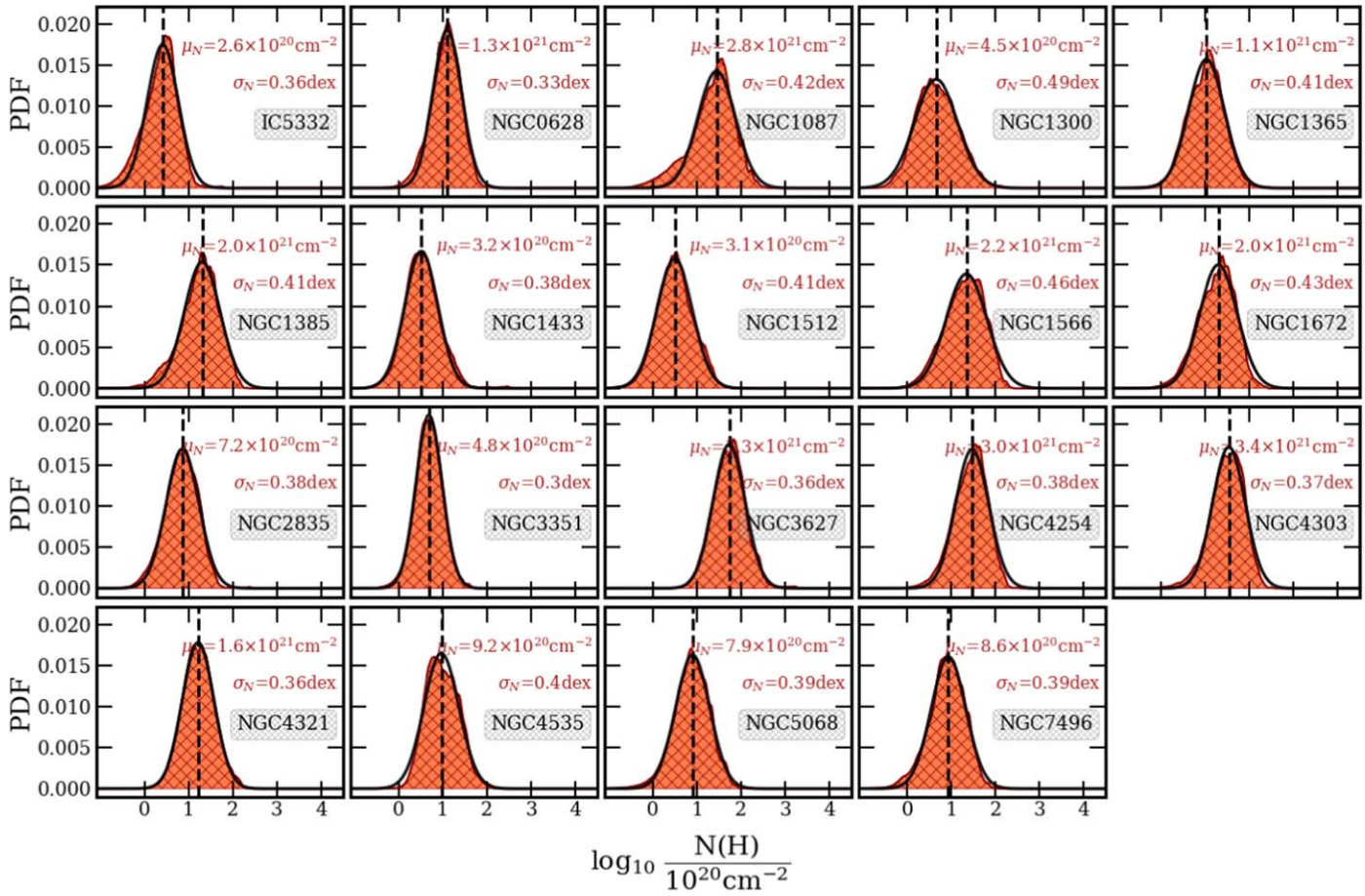

Figure 17. The PDFs of gas column density N(H) in diffuse regions (hatched red) derived from 7.7 μm intensities (Equations (13) and (14)) for each galaxy. Lognormal fits to each of the PDFs with the fit means are overlaid in black for comparison. The best-fit lognormal mean N(H) (μ_N) and dispersion (σ_N) are included, as in Table 2.

Table 4
Summary of N(H)-PDF Parameters

Best-fit Parameter	Median	Q1/Q3	$\pm1\sigma$
Lognormal mean μ_N	11	6/21	12
Lognormal dispersion σ_N	0.39	0.36/0.41	0.04
Mach number $\mathcal{M}$	10.21	8.44/11.86	3.63

Note. Median, first/third quartiles, and standard deviation of the best-fit lognormal mean μ_N in units of 10^{20} cm^{-2} and dispersion σ_N in dex of column density PDFs in the diffuse ISM, and derived isothermal turbulent Mach number $\mathcal{M}$.

which neglects any contribution from the magnetic field and assumes a natural mix of compressive and solenoidal driving modes (see Molina et al. 2012). The spatial scales associated with the Mach numbers we derive from the PDF widths correspond to the galactic scales included in Table 1, which allow us to be agnostic about the turbulent driving scale.

Equation (16) describes the volume density distribution. Following Thompson & Krumholz (2016), this relationship transforms to an analogous expression relating the dispersion of the projected 2D gas column density PDFs, σ_N, to $\mathcal{M}$ given by

$$\sigma^2_{\ln N} \approx \ln(1 + R\mathcal{M}^2/4), \quad \text{or,} \tag{17}$$

$$\sigma_{\log N} \approx 0.43\sqrt{\ln(1 + R\mathcal{M}^2/4)}. \tag{18}$$

Here R is essentially a conversion factor between 3D and 2D column densities of the form (Thompson & Krumholz 2016)

$$R = \frac{1}{2}\left(\frac{3-\alpha}{2-\alpha}\right)\left[\frac{1-\mathcal{M}^{2(2-\alpha)}}{1-\mathcal{M}^{2(3-\alpha)}}\right], \tag{19}$$

where α is the index of the underlying 3D density power spectrum. For $\mathcal{M} \gg 1$ (supersonic turbulence), $\alpha \approx 2.5$ (for a summary, see Krumholz 2014, and references therein). Since most astrophysical systems, including turbulent gas in the ISM of galaxies, have $M \gg 1$, we take $\alpha = 2.5$ as our standard value. Using $\alpha = 2.5$ simplifies Equation (19) to an analytic form, using which $\mathcal{M}$ for isothermal turbulence can be estimated as

$$\mathcal{M} \approx 8[\exp(\sigma^2_{\log_{10} N}/0.18) - 1]. \tag{20}$$

Note that although the location of the peak in the column density PDF depends on whether one is weighting by area or by mass, the dispersion of the PDF is insensitive to this choice (see, e.g., Thompson & Krumholz 2016). Thus, Equation (19) should apply to our mass-weighted column density PDFs.

We consider that these inferred Mach numbers are most likely to be upper limits. The widths of the measured PDFs may be due to a variety of factors other than turbulence. For example, the gas column density may be shaped by bulk flows and galaxy dynamics or large-scale regional variations in the gas surface density (e.g., due to the exponential disk). Any

noncircular flow or motion in the disk environment can contribute to observed velocity dispersions, which is present even where the rotation curve shear is zero (see, e.g., Meidt et al. 2018).

Alternatively our inference of gas column density may be too simplistic, so that we conflate, e.g., variations in the radiation field with column density variations. Formally, our estimate does not *have* to be a lower limit; for example, if variations in the gas column density and radiation field anticorrelate, then the width of the observed PDF might be suppressed, and as mentioned above, we have neglected any impact of magnetic fields.

We also note that Equations (16)–(19) formally apply to isothermal turbulence but that the dust is likely mixed with a wide range of ISM phases spanning some temperature range (e.g., the cold molecular phase has $T \sim 20$ K, while the warm neutral medium has $T \sim 5000$ K). If most of the dust in these regions is with associated cold neutral atomic gas ($T \lesssim 250$ K; Murray et al. 2018) or molecular gas ($T \lesssim 50$ K), we expect these relations to at least approximately hold.

With these caveats in mind, applying Equation (20) to the widths in Table 2 suggests likely upper bounds to the mean Mach numbers of order $\mathcal{M} = 5$–15. The estimated mean Mach numbers are summarized in Table 4. These are in good agreement with what one would estimate contrasting the sound speeds implied by $T \sim 20$ K molecular gas or $T \sim 200$ K cold atomic gas with the observed velocity dispersion of $\sim$3–10 km s^{-1} for molecular gas (e.g., Sun et al. 2020; Rosolowsky et al. 2021) or $\sim$10 km s^{-1} for atomic gas (e.g., Tamburro et al. 2009). Thus, despite a fair number of caveats, it seems reasonable that the width of the approximately lognormal column density distribution that we measure does appear roughly consistent with expectations from isothermal turbulence.

6. Summary

In this paper, we present for the first time the PDFs of mid-IR intensity at an angular resolution of $0\farcs3 - 0\farcs85$ (corresponding to a physical resolution of 20–80 pc) for a representative sample of nearby low-inclination star-forming galaxies with multiwavelength coverage (Section 2). We compare the PDFs across the first 19 PHANGS galaxies observed with JWST-MIRI at 7.7, 10, 11.3, and 21 μm (Section 3). Together this wavelength range captures stochastic emission from small dust grains, including PAHs, as well as thermal emission from the dust continuum. We decompose these PDFs into emission from the galactic centers and galactic disks (Sections 3.2, 3.3). We then parameterize and find the components of the PDFs of the galactic disks using MUSE Hα-identified H II regions (Section 3.4) as follows:

1. The disks of nearby star-forming galaxies show consistent PDF shapes in the mid-IR with an approximately lognormal component that peaks at lower intensities and a power-law tail that emerges at higher intensities (Section 3.4).
2. Based on optically identified H II regions, the power-law component traces emission from H II regions, while the lognormal component results from the emission from the diffuse ISM (Figures 6 and 7).
3. We provide the relative flux fractions and typical range of mid-IR intensities for the galactic centers, disk H II regions, and diffuse emission for all 19 galaxies (Section 3.6).
4. We compute correlations between the intensity PDF components and global properties of our targets (Section 3.8). The diffuse lognormal component correlates strongly with the SFR and gas surface density, while the H II region power-law index shows a moderate correlation with H II region luminosity function slopes.
5. The H II region component (power law) is most prominent (shallowest) and extended at 21 μm, which traces thermal emission from dust grains that survive in H II regions (Section 4.1). The power law slope captures a convolution of the H II region luminosity function and size–luminosity relation.
6. We use the emission at 21 μm to estimate the distribution of luminosity surface densities and show that most H II regions remain well below the typical Eddington luminosity surface density in star formation regions (Section 4.2). We find typical 21 μm intensities in H II regions of about 10 MJy sr^{-1} and bolometric luminosity surface densities of about 225 $L_\odot$ pc^{-2}.
7. Diffuse region PDFs (lognormal) show higher mean intensities at 7.7 and 11.3 μm, due to PAH emission, and an overall depression at the continuum-tracing 10 and 21 μm filters (Section 3.4).
8. The shape of the diffuse PDF remains strikingly lognormal across our full sample of galaxies that span the star-forming main sequence (Figures 16 and 8; Table 3). While the mean varies as a function of environment and band, the lognormal dispersion (width) remains generally consistent in the mid-IR across our full sample ($0.3\ \mathrm{dex} \lesssim \sigma \lesssim 0.4\ \mathrm{dex}$).
9. We leverage the tight correlation between 7.7 μm emission and tracers of gas column density to construct unprecedented high resolution ($0\farcs269$) PDFs of projected gas column density in the diffuse ISM of nearby galaxies (Section 5.1). We find median column densities of order 10^{21} cm^{-2} (Table 2, Figure 17).
10. Assuming that the full width of the gas column density PDFs can be attributed to isothermal turbulence, we measure isothermal turbulent Mach numbers (upper limits) of order 8–15 in diffuse regions (Section 5.3).

Acknowledgments

We thank the anonymous referee for their thoughtful and constructive feedback, which greatly improved the paper.

This work was carried out as part of the PHANGS collaboration.

D.P. gratefully acknowledges support from the NSF GRFP.

A.K.L. gratefully acknowledges support by grants 1653300 and 2205628 from the National Science Foundation, by award JWST-GO-02107.009-A, and by a Humboldt Research Award from the Alexander von Humboldt Foundation.

L.A.L. acknowledges support by the Heising-Simons Foundation and the Simons Foundation. This work was performed in part at the Simons Foundation Flatiron Institute's Center for Computational Astrophysics during L.A.L.'s time as an IDEA Scholar.

J.S. acknowledges support by the Natural Sciences and Engineering Research Council of Canada (NSERC) through a

Canadian Institute for Theoretical Astrophysics (CITA) National Fellowship.

M.B. gratefully acknowledges support from the ANID BASAL project FB210003 and from the FONDECYT regular grant 1211000.

J.C. acknowledges funding from the Belgian Science Policy Office (BELSPO) through the PRODEX project JWST/MIRI Science exploitation (C4000142239).

M.C. and L.R. gratefully acknowledge funding from the DFG through an Emmy Noether Research Group (grant No. CH2137/1-1). COOL Research DAO is a Decentralized Autonomous Organization supporting research in astrophysics aimed at uncovering our cosmic origins.

E.W.K. acknowledges support from the Smithsonian Institution as a Submillimeter Array (SMA) Fellow and the Natural Sciences and Engineering Research Council of Canada.

T.G.W. acknowledges funding from the European Research Council (ERC) under the European Union's Horizon 2020 research and innovation program (grant agreement No. 694343).

F.B. would like to acknowledge funding from the European Research Council (ERC) under the European Union's Horizon 2020 research and innovation program (grant agreement No.726384/Empire).

E.R. acknowledges the support of the Natural Sciences and Engineering Research Council of Canada (NSERC), funding reference No. RGPIN-2022-03499.

K.M.S. and J.S. acknowledge the support of JWST-GO-02107.006-A.

This work uses observations made with the NASA/ESA/CSA James Webb Space Telescope. The data were obtained from the Mikulski Archive for Space Telescopes at the Space Telescope Science Institute, which is operated by the Association of Universities for Research in Astronomy, Inc., under NASA contract NAS 5-03127 for JWST. These observations are associated with program 2017. The specific observations analyzed can be accessed via 10.17909/9bdf-jn24.

Also based on observations collected at the European Southern Observatory under ESO programs 094.C-0623 (PI: Kreckel), 095.C-0473, 098.C-0484 (PI: Blanc), 1100.B-0651 (PHANGS-MUSE; PI: Schinnerer), as well as 094.B-0321 (MAGNUM; PI: Marconi), 099.B-0242, 0100.B-0116, 098.B-0551 (MAD; PI: Carollo), and 097.B-0640 (TIMER; PI: Gadotti).

Facilities: JWST, VLT/MUSE.

Software: astropy (Astropy Collaboration et al. 2013, 2018).

Appendix A
Full Sample MIRI Images and PDFs

This appendix presents the mid-IR images and corresponding PDFs of the full PHANGS-JWST Cycle 1 sample of 19 galaxies (Lee et al. 2023). These are displayed in the figure set available in the online journal and in the example Figure 18, where the top panels show JWST-MIRI images of the galactic disks at 7.7, 10, 11.3, and 21 μm, convolved to $0\farcs85$, with VLT-MUSE-identified H II regions overlaid in cyan. Our analysis is restricted to the footprint of VLT-MUSE Hα mapping for each target (Emsellem et al. 2022). The middle panels show the PDFs of the entire footprint (centers and disks) in fainter dashed lines and the PDFs of the galactic disks overlaid in bold. The PDFs of emission from H II regions and the diffuse ISM are shown as blue and orange hatched regions, respectively. Finally, the bottom panels show the same PDFs in log-stretch. As argued in Section 3.4, the PDFs of galactic disks are separable into a power-law component from H II regions and a lognormal component from diffuse regions.

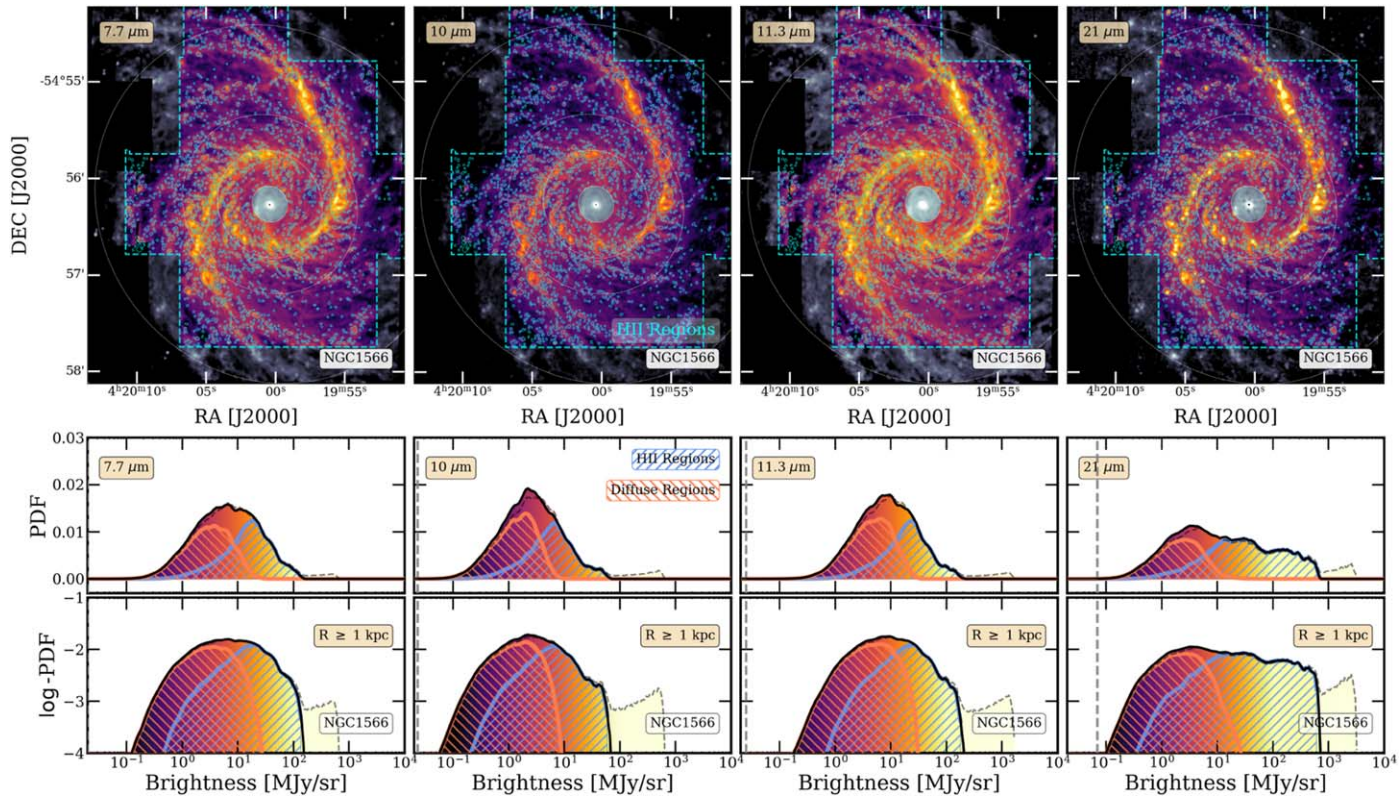

Figure 18. Mid-IR images and PDFs of emission of the galactic disk at 7.7, 10, 11.3, and 21 μm, respectively, for NGC 1566. The complete figure set (19 images) showing the PDFs and mid-IR images for the full PHANGS-JWST Cycle 1 sample is available in the online version of this article.

(The complete figure set (19 images) is available.)

Appendix B
Resolution and PDF Stability

This appendix checks the stability of the diffuse component PDFs with change in resolution. We mask out the contributions from H II regions at native F770W resolution (0.″269) and check how stable the lognormal component is with change in resolution. We compare the lognormal mean μ and dispersion σ across the images of diffuse emission convolved from the native F770W resolution to successively blurred Gaussian PSFs down to 8.″0 with uniform 0.″02 steps.

As seen in Figure 19, while the diffuse intensity PDFs remain generally stable with changes in resolution down to 4.″0, with large changes in resolution, the lognormal component gradually becomes less smooth, the mean shifts to lower intensities, and the PDFs become narrower. Figure 20 shows the same trend for the PDFs of N(H).

Both PDFs only show <4% change in lognormal mean (μ, μ_N) and <7% change in lognormal dispersion (σ, σ_N) in the ∼0.″3–1.″0 range, as summarized in Figure 21. Hence, our diffuse lognormal PDFs of intensity and gas column density remain reliably stable over the 0.″269–0.″85 resolution range where we present results.

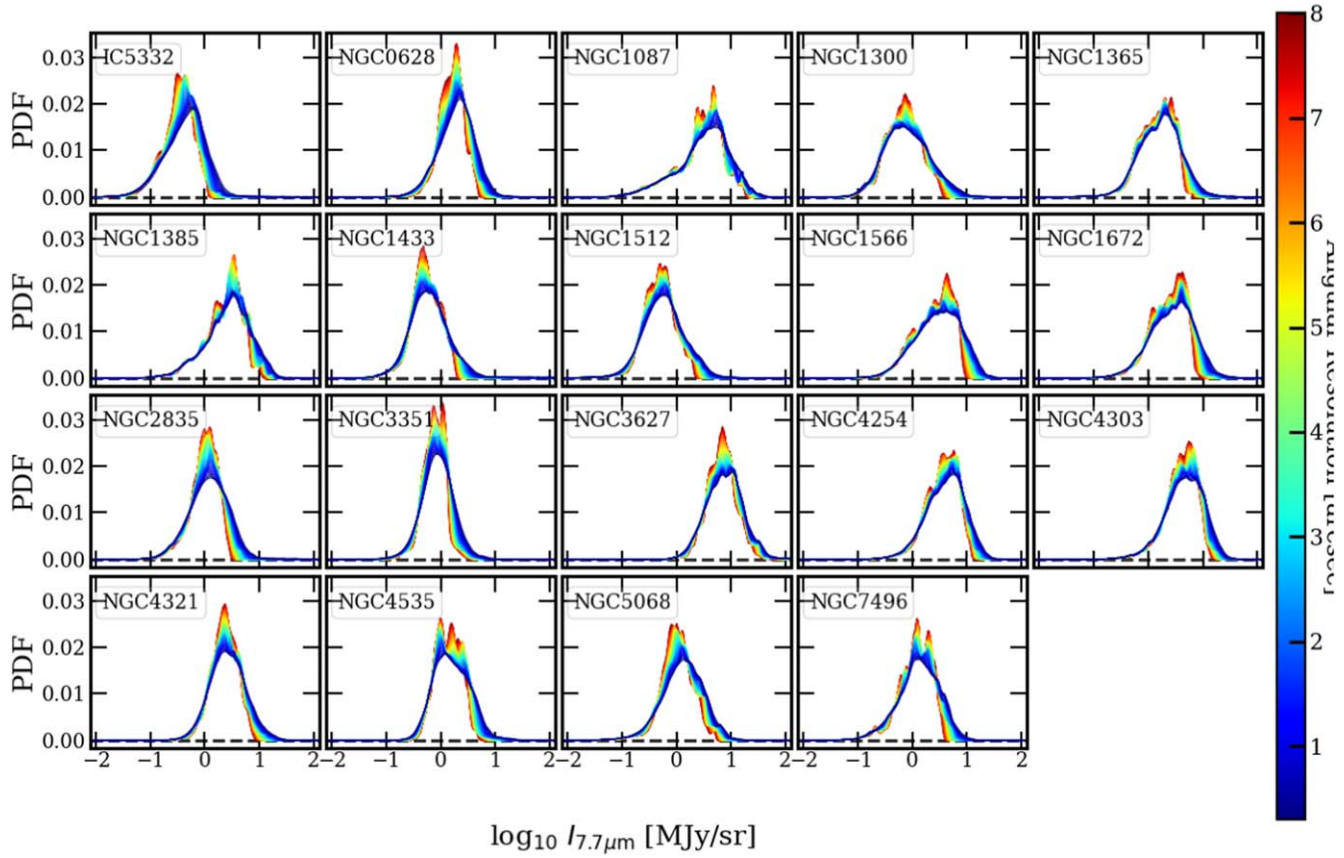

Figure 19. The PDFs of $I_{\rm F770W}$ across different resolutions from native F770W ($0\farcs269$) down to $8\farcs0$ for each target. The PDFs are colored by the FWHM of the Gaussian PSF at each resolution. With lower resolution, the overall PDFs become narrower and shift to lower intensities.

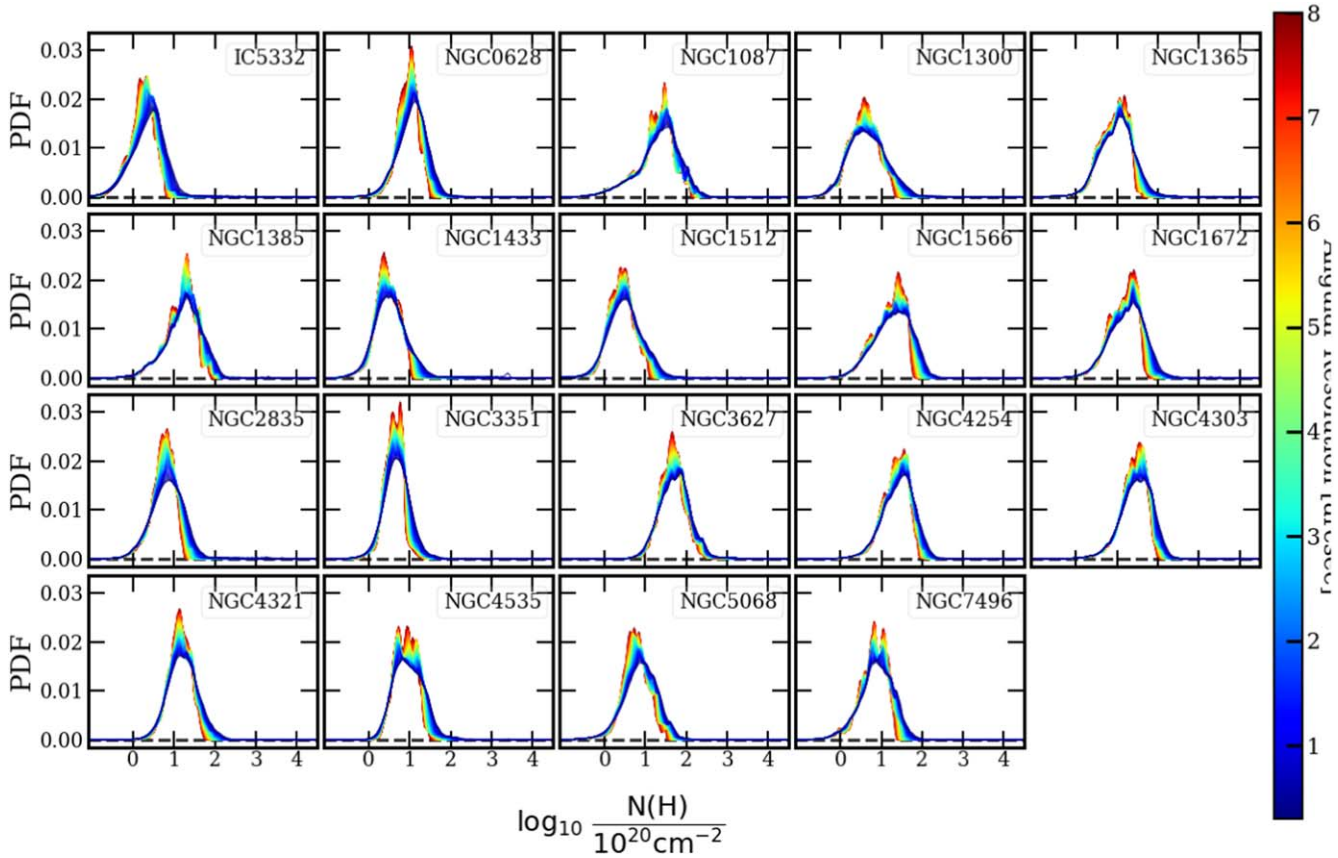

Figure 20. The PDFs of N(H) across different resolutions from native F770W ($0\farcs269$) down to $8\farcs0$ for each target. The PDFs are colored by the FWHM of the Gaussian PSF at each resolution. With lower resolution, the overall PDFs become narrower and shift to lower column densities.

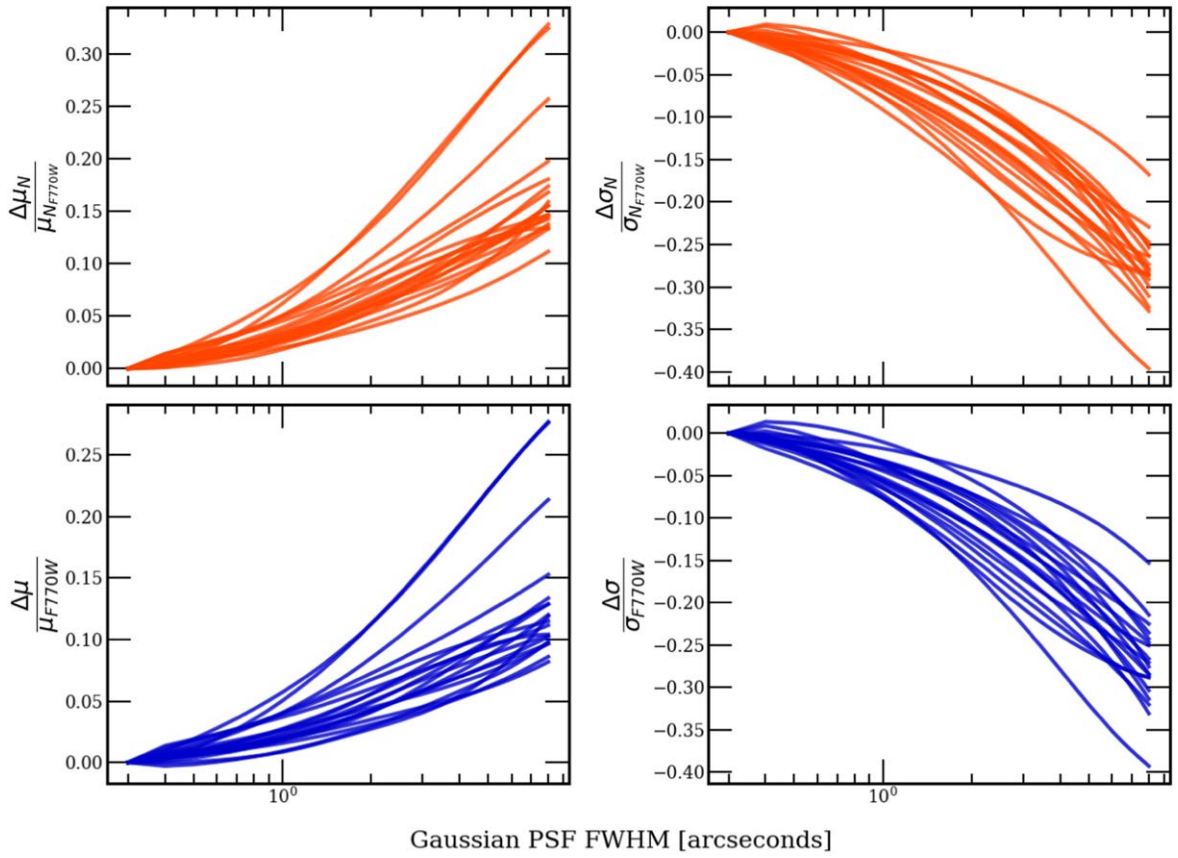

Figure 21. Summarizing the fractional variation in diffuse column density PDF mean (μ_N) and dispersion (σ_N) and in diffuse F770W emission PDF mean (μ) and dispersion (σ).

ORCID iDs

Debosmita Pathak https://orcid.org/0000-0003-2721-487X
Adam K. Leroy https://orcid.org/0000-0002-2545-1700
Todd A. Thompson https://orcid.org/0000-0003-2377-9574
Laura A. Lopez https://orcid.org/0000-0002-1790-3148
Francesco Belfiore https://orcid.org/0000-0002-2545-5752
Médéric Boquien https://orcid.org/0000-0003-0946-6176
Daniel A. Dale https://orcid.org/0000-0002-5782-9093
Simon C. O. Glover https://orcid.org/0000-0001-6708-1317
Ralf S. Klessen https://orcid.org/0000-0002-0560-3172
Eric W. Koch https://orcid.org/0000-0001-9605-780X
Erik Rosolowsky https://orcid.org/0000-0002-5204-2259
Karin M. Sandstrom https://orcid.org/0000-0002-4378-8534
Eva Schinnerer https://orcid.org/0000-0002-3933-7677
Rowan Smith https://orcid.org/0000-0002-0820-1814
Jiayi Sun https://orcid.org/0000-0003-0378-4667
Jessica Sutter https://orcid.org/0000-0002-9183-8102
Thomas G. Williams https://orcid.org/0000-0002-0012-2142
Frank Bigiel https://orcid.org/0000-0003-0166-9745
Yixian Cao https://orcid.org/0000-0001-5301-1326
Jérémy Chastenet https://orcid.org/0000-0002-5235-5589
Mélanie Chevance https://orcid.org/0000-0002-5635-5180
Ryan Chown https://orcid.org/0000-0001-8241-7704
Eric Emsellem https://orcid.org/0000-0002-6155-7166
Christopher M. Faesi https://orcid.org/0000-0001-5310-467X
Kirsten L. Larson https://orcid.org/0000-0003-3917-6460
Sharon Meidt https://orcid.org/0000-0002-6118-4048
Eve C. Ostriker https://orcid.org/0000-0002-0509-9113
Lise Ramambason https://orcid.org/0000-0002-9190-9986
Sumit K. Sarbadhicary https://orcid.org/0000-0002-4781-7291
David A. Thilker https://orcid.org/0000-0002-8528-7340

References

Anand, G. S., Lee, J. C., Van Dyk, S. D., et al. 2021, MNRAS, 501, 3621
Aniano, G., Draine, B. T., Gordon, K. D., & Sandstrom, K. 2011, PASP, 123, 1218
Aniano, G., Draine, B. T., Hunt, L. K., et al. 2020, ApJ, 889, 150
Appel, S. M., Burkhart, B., Semenov, V. A., Federrath, C., & Rosen, A. L. 2022, ApJ, 927, 75
Armus, L., Charmandaris, V., Bernard-Salas, J., et al. 2007, ApJ, 656, 148
Astropy Collaboration, Price-Whelan, A. M., Sipőcz, B. M., et al. 2018, AJ, 156, 123
Astropy Collaboration, Robitaille, T. P., Tollerud, E. J., et al. 2013, A&A, 558, A33
Banfi, M., Rampazzo, R., Chincarini, G., & Henry, R. B. C. 1993, A&A, 280, 373
Belfiore, F., Leroy, A. K., Williams, T. G., et al. 2023, A&A, 678, A129
Bendo, G. J., Draine, B. T., Engelbracht, C. W., et al. 2008, MNRAS, 389, 629
Berkhuijsen, E. M., & Fletcher, A. 2008, MNRAS, 390, L19
Berkhuijsen, E. M., & Fletcher, A. 2015, MNRAS, 448, 2469
Binder, B. A., & Povich, M. S. 2018, ApJ, 864, 136
Blackstone, I., & Thompson, T. A. 2023, MNRAS, 523, 4309
Boersma, C., Bregman, J., & Allamandola, L. J. 2016, ApJ, 832, 51
Bolatto, A. D., Wolfire, M., & Leroy, A. K. 2013, ARA&A, 51, 207
Brunt, C. M., Federrath, C., & Price, D. J. 2010, MNRAS, 403, 1507
Burkhart, B. 2018, ApJ, 863, 118
Burkhart, B., Lee, M.-Y., Murray, C. E., & Stanimirović, S. 2015, ApJL, 811, L28

Burkhart, B., Stalpes, K., & Collins, D. C. 2017, ApJL, 834, L1
Buta, R. J., Sheth, K., Athanassoula, E., et al. 2015, ApJS, 217, 32
Calzetti, D. 2001, PASP, 113, 1449
Calzetti, D., Kennicutt, R. C., Engelbracht, C. W., et al. 2007, ApJ, 666, 870
Calzetti, D., Kennicutt, R. C. J., & Bianchi, J. 2005, ApJ, 633, 871
Chabrier, G. 2003, PASP, 115, 763
Chastenet, J., Sutter, J., Sandstrom, K., et al. 2023a, ApJL, 944, L11
Chastenet, J., Sutter, J., Sandstrom, K., et al. 2023b, ApJL, 944, L12
Chen, H. H.-H., Burkhart, B., Goodman, A., & Collins, D. C. 2018, ApJ, 859, 162
Chevance, M., Kruijssen, J. M. D., Hygate, A. P. S., et al. 2020, MNRAS, 493, 2872
Chown, R., Li, C., Parker, L., et al. 2021, MNRAS, 500, 1261
Churchwell, E., Babler, B. L., Meade, M. R., et al. 2009, PASP, 121, 213
Compiègne, M., Flagey, N., Noriega-Crespo, A., et al. 2010, ApJL, 724, L44
Corbelli, E., Elmegreen, B. G., Braine, J., & Thilker, D. 2018, A&A, 617, A125
Dale, D. A., Helou, G., Contursi, A., Silbermann, N. A., & Kolhatkar, S. 2001, ApJ, 549, 215
Dale, D. A., Helou, G., Silbermann, N. A., et al. 1999, AJ, 118, 2055
de Vaucouleurs, G., de Vaucouleurs, A., Corwin, & Herold, G. 1991, Third Reference Catalogue of Bright Galaxies (New York: Springer)
den Brok, J. S., Chatzigiannakis, D., Bigiel, F., et al. 2021, MNRAS, 504, 3221
Draine, B. T. 2011, Physics of the Interstellar and Intergalactic Medium (Princeton, NJ: Princeton Univ. Press)
Draine, B. T., Dale, D. A., Bendo, G., et al. 2007, ApJ, 663, 866
Draine, B. T., & Li, A. 2001, ApJ, 551, 807
Draine, B. T., & Li, A. 2007, ApJ, 657, 810
Egorov, O. V., Kreckel, K., Sandstrom, K. M., et al. 2023, ApJL, 944, L16
Emsellem, E., Schinnerer, E., Santoro, F., et al. 2022, A&A, 659, A191
Federrath, C., & Klessen, R. S. 2013, ApJ, 763, 51
Federrath, C., Klessen, R. S., & Schmidt, W. 2008, ApJL, 688, L79
Federrath, C., Roman-Duval, J., Klessen, R. S., Schmidt, W., & Mac Low, M. M. 2010, A&A, 512, A81
Galametz, M., Kennicutt, R. C., Calzetti, D., et al. 2013, MNRAS, 431, 1956
Galliano, F., Galametz, M., & Jones, A. P. 2018, ARA&A, 56, 673
Galliano, F., Madden, S. C., Tielens, A. G. G. M., Peeters, E., & Jones, A. P. 2008, ApJ, 679, 310
Girichidis, P., Konstandin, L., Whitworth, A. P., & Klessen, R. S. 2014, ApJ, 781, 91
Glover, S. C. O., Federrath, C., Mac Low, M. M., & Klessen, R. S. 2010, MNRAS, 404, 2
Goodman, A. A., Pineda, J. E., & Schnee, S. L. 2009, ApJ, 692, 91
Groves, B., Kreckel, K., Santoro, F., et al. 2023, MNRAS, 520, 4902
Hao, L., Spoon, H. W. W., Sloan, G. C., et al. 2005, ApJL, 625, L75
Hassani, H., Rosolowsky, E., Leroy, A. K., et al. 2023, ApJL, 944, L21
Hennebelle, P., & Falgarone, E. 2012, A&ARv, 20, 55
Hoffmann, K. H., Essex, C., Basu, S., & Prehl, J. 2018, MNRAS, 478, 2113
Hoyer, N., Pinna, F., Kamlah, A. W. H., et al. 2023, ApJL, 944, L25
Hunt, L. K., Draine, B. T., Bianchi, S., et al. 2015, A&A, 576, A33
Imara, N., & Burkhart, B. 2016, ApJ, 829, 102
Kainulainen, J., Federrath, C., & Henning, T. 2014, Sci, 344, 183
Kim, J., Chevance, M., Kruijssen, J. M. D., et al. 2022, MNRAS, 516, 3006
Klessen, R. S., & Burkert, A. 2000, ApJS, 128, 287
Klessen, R. S., & Glover, S. C. O. 2016, in Star Formation in Galaxy Evolution: Connecting Numerical Models to Reality (Saas-Fee Advanced Course) Vol. 43, ed. Y. Revaz et al. (Berlin: Springer-Verlag), 85
Klessen, R. S., Heitsch, F., & Mac Low, M.-M. 2000, ApJ, 535, 887
Kreckel, K., Ho, I. T., Blanc, G. A., et al. 2019, ApJ, 887, 80
Kruijssen, J. M. D., Schruba, A., Chevance, M., et al. 2019, Natur, 569, 519
Krumholz, M. R. 2014, PhR, 539, 49
Krumholz, M. R., McKee, C. F., & Bland-Hawthorn, J. 2019, ARA&A, 57, 227
Lada, C. J., Lewis, J. A., Lombardi, M., & Alves, J. 2017, A&A, 606, A100
Lai, T. S. Y., Armus, L., Bianchin, M., et al. 2023, ApJL, 957, L26
Lang, P., Meidt, S. E., Rosolowsky, E., et al. 2020, ApJ, 897, 122
Lawton, B., Gordon, K. D., Babler, B., et al. 2010, ApJ, 716, 453
Lee, J. C., Sandstrom, K. M., Leroy, A. K., et al. 2023, ApJL, 944, L17
Leroy, A. K., Rosolowsky, E., Usero, A., et al. 2022, ApJ, 927, 149
Leroy, A. K., Sandstrom, K., Rosolowsky, E., et al. 2023, ApJL, 944, L9
Leroy, A. K., Schinnerer, E., Hughes, A., et al. 2021, ApJS, 257, 43
Li, A., & Draine, B. T. 2001, ApJ, 554, 778
Li, Y., Calzetti, D., Kennicutt, R. C., et al. 2010, ApJ, 725, 677
Li, Y., Klessen, R. S., & Mac Low, M.-M. 2003, ApJ, 592, 975
Liu, D., Schinnerer, E., Cao, Y., et al. 2023, ApJL, 944, L19
Lombardi, M., Alves, J., & Lada, C. J. 2015, A&A, 576, L1
Makarov, D., Prugniel, P., Terekhova, N., Courtois, H., & Vauglin, I. 2014, A&A, 570, A13
Mascoop, J. L., Anderson, L. D., Wenger, T. V., et al. 2021, ApJ, 910, 159
Mathis, J. S., Mezger, P. G., & Panagia, N. 1983, A&A, 128, 212
Meidt, S. E., Leroy, A. K., Rosolowsky, E., et al. 2018, ApJ, 854, 100
Molina, F. Z., Glover, S. C. O., Federrath, C., & Klessen, R. S. 2012, MNRAS, 423, 2680
Murray, C. E., Stanimirović, S., Goss, W. M., et al. 2018, ApJS, 238, 14
Onodera, S., Kuno, N., Tosaki, T., et al. 2010, ApJL, 722, L127
Ostriker, E. C., Stone, J. M., & Gammie, C. F. 2001, ApJ, 546, 980
Padoan, P., Federrath, C., Chabrier, G., et al. 2014, in Protostars and Planets VI, ed. H. Beuther et al. (Tucson, AZ: Univ. Arizona Press), 77
Padoan, P., & Nordlund, A. 2002, ApJ, 576, 870
Pan, H.-A., Schinnerer, E., Hughes, A., et al. 2022, ApJ, 927, 9
Paradis, D., Reach, W. T., Bernard, J.-P., et al. 2009, AJ, 138, 196
Peeters, E., Spoon, H. W. W., & Tielens, A. G. G. M. 2004, ApJ, 613, 986
Perrin, M. D., Sivaramakrishnan, A., Lajoie, C.-P., et al. 2014, Proc. SPIE, 9143, 91433X
Pontoppidan, K. M., Barrientes, J., Blome, C., et al. 2022, ApJL, 936, L14
Portegies Zwart, S. F., McMillan, S. L. W., & Gieles, M. 2010, ARA&A, 48, 431
Querejeta, M., Schinnerer, E., Meidt, S., et al. 2021, A&A, 656, A133
Relaño, M., De Looze, I., Kennicutt, R. C., et al. 2018, A&A, 613, A43
Relaño, M., & Kennicutt, R. C. J. 2009, ApJ, 699, 1125
Rigby, J. R., Lightsey, P. A., García Marín, M., et al. 2023, PASP, 135, 048002
Rigopoulou, D., Barale, M., Clary, D. C., et al. 2021, MNRAS, 504, 5287
Rosolowsky, E. 2005, PASP, 117, 1403
Rosolowsky, E., Hughes, A., Leroy, A. K., et al. 2021, MNRAS, 502, 1218
Sandstrom, K. M., Koch, E. W., Leroy, A. K., et al. 2023, ApJL, 944, L8
Sandstrom, K. M., Leroy, A. K., Walter, F., et al. 2013, ApJ, 777, 5
Santoro, F., Kreckel, K., Belfiore, F., et al. 2022, A&A, 658, A188
Schinnerer, E., Emsellem, E., Henshaw, J. D., et al. 2023, ApJL, 944, L15
Schneider, N., Ossenkopf-Okada, V., Clarke, S., et al. 2022, A&A, 666, A165
Schruba, A., Leroy, A. K., Walter, F., Sandstrom, K., & Rosolowsky, E. 2010, ApJ, 722, 1699
Smith, J. D. T., Draine, B. T., Dale, D. A., et al. 2007, ApJ, 656, 770
Smith, R. J., Tress, R., Soler, J. D., et al. 2023, MNRAS, 524, 873
Sormani, M. C., Barnes, A. T., Sun, J., et al. 2023, MNRAS, 523, 2918
Spoon, H. W. W., Marshall, J. A., Houck, J. R., et al. 2007, ApJL, 654, L49
Sun, J., Leroy, A. K., Ostriker, E. C., et al. 2020, ApJ, 892, 148
Sun, J., Leroy, A. K., Rosolowsky, E., et al. 2022, AJ, 164, 43
Tamburro, D., Rix, H. W., Leroy, A. K., et al. 2009, AJ, 137, 4424
Thompson, T. A., & Krumholz, M. R. 2016, MNRAS, 455, 334
Tielens, A. G. G. M. 2008, ARA&A, 46, 289
Vázquez-Semadeni, E., & García, N. 2001, ApJ, 557, 727
Veron-Cetty, M. P., & Veron, P. 2010, A&A, 518, A10
Whitcomb, C. M., Sandstrom, K., Leroy, A., & Smith, J. D. T. 2023a, ApJ, 948, 88
Whitcomb, C. M., Sandstrom, K., & Smith, J.-D. T. 2023b, RNAAS, 7, 38
Yajima, Y., Sorai, K., Miyamoto, Y., et al. 2021, PASJ, 73, 257